Chemical Engineering Journal 485 (2024) 149766

Contents lists available at ScienceDirect

Chemical Engineering Journal

journal homepage: www.elsevier.com/locate/cej

Heterogeneous Fenton oxidation of phenol photo-assisted with visible radiation in the presence of g-C_3N_4 catalysts modified with different iron phases

Evelyn Alejandra Burbano [a], Carlos Andrés Vallejo [a], Juan David Ramirez [b,d], Arsenio Hidalgo-Troya [c], Luis Alejandro Galeano [a,*]

[a] Grupo de Investigación en Materiales Funcionales y Catálisis (GIMFC) 520002 Pasto, Nariño, Colombia
[b] Centro de Investigaciones en Microbiología y Biotecnología-UR (CIMBIUR), Facultad de Ciencias Naturales, Universidad del Rosario, Bogotá 110221, Colombia
[c] Grupo de Investigación Salud Pública, Universidad de Nariño, Pasto 520002, Nariño, Colombia
[d] Molecular Microbiology Laboratory, Department of Pathology, Molecular and Cell-Based Medicine, Icahn School of Medicine at Mount Sinai, New York, NY 10029, USA

ARTICLE INFO

Keywords:
Phenol degradation
Heterogeneous Fenton photo-assisted with visible light
Fe-functionalized graphitic carbon nitride
circumneutral pH

ABSTRACT

This work compared graphitic carbon nitride (g-C_3N_4) modified with different iron phases to maximize its catalytic response in the phenol degradation at circumneutral pH under visible irradiation (Xe lamps, 70 W) and H_2O_2. The semiconductor was modified with different iron phases either: *(i)* supported (Fe^{n+}/g-C_3N_4, Fe_3O_4/g-C_3N_4 and α-Fe_2O_3/g-C_3N_4) or *(ii)* doped (Fe-g-C_3N_4). The materials were characterized by AAS, DRIFTS, DR-UV–Vis, N_2 adsorption, TGA, H_2-TPR, XPS, and XRD. Fe-g-C_3N_4 degraded 85 % of phenol (45 min), mineralized 62 % of DOC (180 min), leaching negligible iron (0.00131 mg Fe/L) at 25.0 ± 0.2 °C and pH 7.0. At pH 3.0, both phenol degradation (90 min) and mineralization (210 min) reached 100 %. The highly specific location of the metal within the lattice of the semiconductor substantially improved the use of the visible-light-photogenerated electron-hole pairs by the heterogeneous Fenton catalytic system in comparison to the metal oxides deposited on its surface.

1. Introduction

Aquatic resources are essential for human life and economic development. However, the contamination of water sources by the discharge of wastewater (WW) is one of the main environmental problems facing the world today [1]. Decontamination of WW before final discharge is crucial to prevent the spread of diseases, avoid damage to natural water sources, and protect public health [2]. Furthermore, its treatment can help reduce the contamination of freshwater sources and improve the availability of water resources in some areas of the planet [1,3]. Many organic contaminants have been reported in WW [4], including phenolic compounds, which can contaminate surface and groundwater [5,6]. These compounds are the least biodegradable, and their long-term accumulation causes serious harm, especially to humans [7].

Advanced oxidation processes (AOPs) have been widely studied due to their ability to significantly degrade and mineralize toxic organic contaminants dissolved in water, including phenolic compounds, contaminants of emerging concern (CECs), and a wide variety of refractory azo dyes [8–12]. The versatility of AOPs comes from the high standard reduction potential of the reactive oxygen species (ROS) generated [10]. In addition to being highly oxidizing, these radical species are not particularly selective, and can be generated from oxidant precursors such as ozone (O_3) or hydrogen peroxide (H_2O_2) [13]. The Fenton process is an advanced oxidation process that can be catalyzed with iron salts or iron-modified solid catalysts in the presence of hydrogen peroxide (H_2O_2). The Fenton process can be carried out in a homogeneous or heterogeneous phase, with the latter variant being more promising for large-scale applications due to the potential reusability of the catalyst and the sustainability of the process [14,15]. The main disadvantages of the homogeneous Fenton process are the need to maintain an acidic pH lower than 4.0 to avoid metal precipitation, and the costly separation of the catalyst from the fluid phase once the reaction is complete, as well as the generation of large quantities of sludge requiring additional treatment [15]. In contrast, photo-assisted

* Corresponding author.
E-mail address: alejandrogaleano@udenar.edu.co (L.A. Galeano).

https://doi.org/10.1016/j.cej.2024.149766
Received 1 December 2023; Received in revised form 30 January 2024; Accepted 15 February 2024
Available online 16 February 2024

heterogeneous Fenton oxidation processes allow organic contaminants present in water to be eliminated more efficiently, even under conditions of circumneutral pH (~ 7.0). This is because they improve the formation of reactive oxygen species and iron can be regenerated more quickly in its lowest oxidation state within the catalytic cycle (Fe^{3+}/Fe^{2+}) [7,16]. Furthermore, this variant of the process is more environmentally sustainable, since it reduces energy consumption if sunlight can be used as an energy source, instead of depending on non-renewable energy sources [17]. Solar radiation is a largely untapped resource in such applications, bearing in mind that the visible region (400 to 700 nm) represents 47.5 % of its total energy [14]. Furthermore, heterogeneous Fenton processes significantly reduce operating costs by facilitating the separation of the catalyst from the reaction system. According to numerous investigations, the most useful and flexible catalysts to apply to photoactivated AOPs are semiconductors [7,18–20]. Recently, different variants of the photo-assisted Fenton process have been reported using solid photocatalysts such as TiO_2, ZnO, $ZnWO_4$, Fe_2O_3/TiO_2, Fe_3O_4/TiO_2 and $ZnFe_2O_4$ [18,21,22], but activity has primarily been limited to the ultraviolet region (UV) between 100 and 400 nm. This due to its characteristic bandgap being close to 3.2 eV which markedly restricts a more complete exploitation of solar radiation. In recent years, there has been a sharp increase in number of scientific publications on graphitic carbon nitride (*g*-C_3N_4), making it an ideal candidate for photocatalytic applications, including photo-assisted AOPs [23]. *g*-C_3N_4 is a metal-free organic semiconductor whose structure is made up of multiple parallel layers of stacked tri-*s*-triazine units [7,20,24]. These characteristics make it a stable and low-toxicity material. Additionally, it has a bandgap of 2.7 eV [23] that allows it to be photoactive in the presence of visible light without having an inflated recombination rate for the photogenerated electron-hole pairs [18]. The preparation of *g*-C_3N_4 can be carried out through thermal treatment of relatively inexpensive nitrogen-rich precursors (like melamine, dicyandiamide, urea, among others), in an inert atmosphere [24,25].

Studies based on *g*-C_3N_4 have focused mainly on trying to reduce the recombination rate of photogenerated electron-hole pairs through different procedures, including the creation of semiconductor–semiconductor or metal–semiconductor heterojunctions to effectively separate electrons and holes, or the doping of *g*-C_3N_4 with metallic elements to act as electron capture centers, leaving highly oxidized holes [18,24,26]. These latest modifications have shown that the incorporation of metal ions (*e.g.* Pd, Fe, Cu, Zn, Ni, etc.) in the polymeric network of the semiconductor improves the useful life of the photocatalyst and the mobility of the charge carriers, while increasing light absorption [23,26]. Studies have been carried out on the modification of graphitic carbon nitride type materials with different iron phases to eliminate a variety of organic contaminants in water, including dyes and phenolic compounds, demonstrating a high photocatalytic response in visible irradiation [7,27–30]. However, to the best of our knowledge, no study has yet been performed to compare the different phases of iron in the degradation of the same contaminant under identical reaction conditions (namely pH, temperature, same oxidizing agent, etc.). It is also worth mentioning that the studies on the photocatalytic activity of this type of materials mostly reported the use persulfate or PMS as an oxidizing agent [31–37]. There is scarce information available on the use of H_2O_2 in this reaction [7,38,39], despite the proven efficiency of Fenton processes in the degradation of all types of contaminants [14,31,40]. Finally, it is important to mention that the existing studies have not evaluated the catalytic potential of these materials under circumneutral pH conditions for purposes of decontamination prior to final discharge into natural bodies of water. Circumneutral pH is common in much of the water supplying surface water treatment plants (for purposes of purification) and in wastewater.

Consequently, this research focused on preparing solid photocatalysts based on graphitic carbon nitride (*g*-C_3N_4) with iron doped structurally or used as a support of different metal phases (Fe^{n+}, Fe_3O_4 and α-Fe_2O_3). All materials were characterized by modern physicochemical techniques to clearly elucidate their structure, and compared based on their catalytic response in the heterogeneous Fenton degradation of Phenol (PhO) photo-assisted with visible light, at circumneutral pH.

2. Experimental

2.1. Materials

The graphitic carbon nitride used as a photocatalytic support was prepared from melamine (99 %, Sigma-Aldrich®). The following materials were prepared: $FeCl_3{\cdot}6H_2O$ (97 %, Panreac®), $FeCl_2{\cdot}4H_2O$ (99 %, Sigma-Aldrich®), $Fe(NO_3)_3{\cdot}9H_2O$ (98 %, Panreac®), anhydrous $FeCl_3$ (97 %, Mexifloc®), absolute ethanol (99.8 %, Honeywell Fluka®), NH_4OH (25 %, Emsure®) and $FeSO_4{\cdot}7H_2O$ (99 %, Panreac®), UAP Nitrogen (99.999 %, Cryogas) and UAP Hydrogen (99.999 %, Cryogas), all without any additional purification. Acid digestion for the elemental analysis of solids was performed using HCl (37 %, Panreac®), $HClO_4$ (70 %, Sigma-Aldrich®) and HNO_3 (65 %, Emsure®, Merck). For the catalytic experiments, phenol (99.0—100 %, Sigma-Aldrich®) and hydrogen peroxide (50 %p/p, Chemí®) were used.

2.2. Preparation of the photocatalytic support

Graphitic carbon nitride was prepared from melamine placed in a crucible semi-closed with a lid and subjected to heat treatment up to 550 °C for 4.0 h, under a heating ramp of 5.0 °C/min in a nitrogen atmosphere (~2.83 L/h N_2 STP). Finally, the material was macerated to a particle size of 210 μm (70 mesh sieve) and placed in a closed container.

2.3. Preparation of the photocatalysts

Four photocatalysts were prepared with identical final nominal iron loading (5.0 w/w % Fe). Three of these were modified with different iron phases on *g*-C_3N_4: *(i)* iron supported on graphitic carbon nitride (Fe^{n+}/*g*-C_3N_4), *(ii)* magnetite supported on graphitic carbon nitride (Fe_3O_4/*g*-C_3N_4), and *(iii)* hematite supported on graphitic carbon nitride (α-Fe_2O_3/*g*-C_3N_4). The fourth *(iv)* was prepared by doping the support with anhydrous iron chloride from its initial preparation (Fe-*g*-C_3N_4). For the photocatalysts *(i)* to *(iii)*, the carbon nitride support (*g*-C_3N_4) was previously suspended by dispersing 5.0 g of *g*-C_3N_4 in 200 mL of a solution of EtOH:H_2O (1:2), and subjected to ultrasound for 2.0 h at room temperature.

(i)* Fe^{n+}/*g*-C_3N_4 *photocatalyst: A solution of $FeSO_4{\cdot}7H_2O$ at 0.1 g of salt/mL of type II water was prepared, and under magnetic stirring the solution was dispersed over the carbon nitride suspension (*g*-C_3N_4). The mixture was stirred continuously until complete evaporation at 110 °C. The solid obtained was then macerated to a particle size of 210 μm (70 mesh sieve), placed in a crucible semi-closed with a lid, and calcined at 500 °C under a ramp of 10.0 °C/min in a hydrogen atmosphere (~2.83 L/h H_2 STP) for 4.0 h to promote the reduction of Fe supported on the surface.

(ii)* Fe_3O_4/*g*-C_3N_4 *photocatalyst: This photocatalyst was prepared by adapting the methodology previously reported by Kumar *et al.* [41]. The $FeCl_3{\cdot}6H_2O$ and $FeCl_2{\cdot}4H_2O$ salts were dissolved separately at 0.1 g of salt/mL of distilled water, maintaining a 2:1 stoichiometric ratio between the Fe^{3+}:Fe^{2+} chlorides. The solutions were added to the carbon nitride (*g*-C_3N_4) suspension under constant stirring and reflux. The system was heated to 80 °C for 0.5. 0.3 mL of NH_4OH (25 %)/mmol Fe was added dropwise to the mixture, and left under stirring and reflux for 0.5 h at 80 °C. Finally, the Fe_3O_4/*g*-C_3N_4 photocatalyst was separated by vacuum filtration, washed several times with type II water and absolute ethanol, and dried for 12 h at 80 °C.

(iii)* α-Fe_2O_3/*g*-C_3N_4 *photocatalyst: This photocatalyst was prepared by adapting the methodology reported by Li *et al.* [42], in which 100 mL of a $FeCl_3{\cdot}6H_2O$ solution (46 mmol/L) was added to 5.0 g of *g*-

C_3N_4. The mixture was dispersed by ultrasound for 10 min, stirred for 30 min at 40 °C, and dried at 50 °C for 2 days. Subsequently, the material was calcined at 430 °C under a ramp of 5.0 °C/min in an oxygen atmosphere (~2.83 L/h O_2 STP) for 4.0 h.

(iv)* Fe-*g*-C_3N_4 *photocatalyst: This photocatalyst was prepared by adapting the methodology previously reported by Hu *et al.* [7]. 5.0 g of melamine were dissolved in 20 mL of water at 80 °C. Anhydrous $FeCl_3$ was added to the dispersion under magnetic stirring and left for 1.0 h at 80 °C. The mixture was then completely evaporated at 120 °C and macerated. The powder was placed in a crucible semi-closed with a lid and calcined at 550 °C at a heating rate of 2.0 °C/min under a nitrogen atmosphere (~2.83 L/h N_2 STP) for 4.0 h.

For comparative purposes, the magnetite (Fe_3O_4) and hematite (α-Fe_2O_3) mass phases were also prepared, maintaining the same heating conditions and calcination atmospheres used in the preparation of their supported photocatalysts.

2.4. Analytical methods

The carbon, hydrogen and nitrogen (CHN) content of the materials was determined by elemental analysis of solids in a Thermo Scientific FlashEA 1112 CHN analyzer. The iron content was determined by atomic absorption spectroscopy (AAS) using an ICE 3500-Series 3000 Thermo Scientific spectrophotometer after acid digestion of the photocatalysts with a 2:1:1 mixture of HCl, $HClO_4$ and HNO_3.

The diffuse reflectance infrared spectroscopy (DRIFTS) spectra of the support and photocatalysts were obtained in the mid wavelength range (4000–400 cm^{-1}) using an IRXross Shimadzu instrument equipped with an accessory to measure in DRS 8000A diffuse reflectance mode. The analyses were performed in transmission mode. The samples were diluted in KBR (1.0 g of sample in 150 mg of KBr).

The powder X-ray diffraction (XRD) patterns of the precursor materials, the photocatalysts and the reference oxides were determined from the powder samples between 10 and 80 °(2θ) in a Bruker D8 Advance diffractometer operated at 40 kV and 30 mA with a scanning speed of 2.5 °(2θ)/min, using filtered CuKα radiation (λ = 1.5406 Å). The average crystallite size for the supported phases of the metal were calculated using the Scherrer equation Eq. (1) with the signal of the most intense peak, for Fe_3O_4 with signal (3 1 1) and for α-Fe_2O_3 with signal (1 0 4), where K is the corresponding dimensionless quantity for each crystalline structure: 0.94 (Fe_3O_4) [43] and 0.9 (α-Fe_2O_3) [44], λ is the wavelength of the incident radiation, β is the full width at half maximum (FWHM) and θ is the diffraction angle.

$$D = \frac{K.\lambda}{\beta.\mathrm{Cos}\theta} \quad (1)$$

The TGA thermal analysis of the *g*-C_3N_4 photocatalytic support, photocatalysts and reference oxides was carried out using a SDT Q600 analyzer from TA Instruments. A heating ramp of 10 °C/min was used under a flow rate of 20 mL/min of chromatographic Zero air (mix of 78.1 % of N_2 99.999 % and 21.9 % of O_2 99.6 ± 0.5 % of absolute precision, Indura Cryogas ®) from 30 °C up to 800 °C.

Hydrogen temperature programmed reduction (H_2-TPR) analyses were carried out in a Micromeritics Chemisorb 2750 analyzer provided with a TPx unit to control the temperature and heating rate. Around 10 to 20 mg of sample were pretreated at 200 °C for 1.0 h in a nitrogen atmosphere and analyzed between 150 °C and 900 °C at 10 °C/min under a total flow of 50 mL/min of the reducing gas (9.78 % H_2/Ar). Hydrogen consumption was recorded using a thermal conductivity detector (TCD) and Ag_2O (99.99 % Fisher Scientific) was used as an external standard for peak area calibration.

The textural analysis of the materials was carried out using nitrogen adsorption/desorption isotherms at −196 °C in a Micromeritics 3-Flex analyzer, in a range of relative pressures from 10^{-3} to 0.99, on samples of around 100 to 200 mg previously degassed at 200 °C for 12 h. The BET specific surface (S_{BET}) was determined using the multipoint model, with the *Keii-Rouquerol* criteria to define the zone with best linearity [45]. The external surface area (S_{ext}) was calculated using the *t-plot* method (Harkins-Jura). The pore size distribution was determined by BJH desorption analysis, using the statistical thickness of Harkins and Jura.

The bandgap of the photocatalysts and the support was calculated by DR UV–Vis spectroscopy using a Shimadzu UV-2600 spectrophotometer provided with an ISR-2600Plus integration sphere in a spectral range between 200 and 1200 nm. Each material was compacted and placed in the sample container of the integration sphere. The bandgap was estimated using the Kubelka-Munk F method Eq. (2), coupled to the graphical method for calculating the bandgap energy (Eg) proposed by Tauc Eq. (3), where α is the absorption coefficient, $h\nu$ is the energy of the photon, A is a constant and $n = ½$ is the allowed direct transition. To estimate the bandgap value from the UV–Vis spectrum, a straight line was extrapolated from the absorption curve $(\alpha h\nu)^2$ to the abscissa axis ($h\nu$) when α had a value of zero and $Eg = h\nu$ [46].

$$(R) = (1-R)^2/2R \approx \alpha \quad (2)$$

$$(\alpha h\nu)^{1/n} = A(h\nu - Eg) \quad (3)$$

The elemental composition was determined at the surface level and the oxidation states of the active metal were estimated by means of X-ray photoelectron spectroscopy (XPS) using a SPECs NAP-XPS system and employing the CasaXPS® Version 2.3.25PR1.0 software to analyze the general spectrum and the high resolution for the most representative signals of Fe^{3+} and Fe^{2+} [47].

2.5. Photocatalytic experiments

The graphitic carbon nitride support and the prepared photocatalysts were evaluated as active solids in the heterogeneous Fenton reaction for the degradation of phenol in UHP water photo-assisted with visible light (Xenon HID bulb light, 35 W, 12 V, 6000 K) [48]. The experiments were carried out at 25.0 ± 0.1 °C and atmospheric pressure (74 kPa) in a 500 mL semi-batch glass reactor (Pyrex®) jacketed to control the temperature, coupled to 2 Xenon lamps of 35 W each, a thermostatic bath, a peristaltic pump to dose H_2O_2 under controlled flow, and a 600 rpm mechanical stirrer. For each test, the reactor was loaded with 350 mL of phenol solution (10 mg/L Dissolved Organic Carbon - DOC equivalent) and 50 mg Fe/L of photocatalyst and set to provide constant air bubbling (2.0 L/min). The pH of the solution was adjusted to 7.0 at the starting point of the reaction by adding HCl or 0.1 M NaOH dropwise. Xenon lamps were switched on and H_2O_2 solution (1.94 mmol/L, equivalent to the theoretical stoichiometric amount necessary for complete mineralization of phenol), was added after 30 min of stirring and air bubbling (equilibration period) under a flow rate of 50 mL/h. Zero time of reaction began by adding the hydrogen peroxide solution to the reactor, after which 15.0 mL samples were taken every 45 min for a total reaction time of 3.0 h. Once the addition of H_2O_2 was complete, the system was irradiated for additional 30 min, maintaining constant stirring and bubbling, and a final sample of 15.0 mL was taken 4.0 h after the photocatalytic test had started. Each sample was microfiltered (0.45 μm, Millipore) to remove the dispersed photocatalyst before analysis. In each experiment, the concentration of phenol was monitored using high-efficiency liquid chromatography (HPLC-PDA, Prominence Shimadzu) to calculate the level of degradation and Dissolved Organic Carbon to calculate the extent of carbon mineralization (TOC-L CPH, Shimadzu analyzer). At the end of each catalytic test, the chemical stability of the active metal in the photocatalyst was checked by determining the concentration of dissolved iron in the reaction's effluent using atomic absorption spectroscopy (AAS). Finally, in the presence of the best photocatalyst, five sequential reuse catalytic cycles were performed to assess its catalytic stability and reusability over time. After each cycle, the photocatalyst was recovered through vacuum filtration, washed

three times with deionized water, and dried in a vacuum drying oven at 60 °C.

3. Results and discussion

3.1. Physicochemical characteristics of the photocatalysts

It was possible to obtain materials with yields greater than 25.0 % (Table 1). Compared to the small quantity of results available in the literature that report yields in the preparation of this type of photoactive material, the results of this study are among the highest achieved. In general, yields reported using thermal polymerization range from 4 % to 50 % [49–51]. The magnetite and hematite phases supported on carbon nitride ($Fe_3O_4/g\text{-}C_3N_4$ and $\alpha\text{-}Fe_2O_3/g\text{-}C_3N_4$) obtained yields of 51.9 % and 44.2 %, respectively. The high yield for $Fe_3O_4/g\text{-}C_3N_4$ can be attributed to the methodology used in the preparation of the material, in which 80 °C was not exceeded. The yield of the Fe-$g\text{-}C_3N_4$ photocatalyst (49.5 %) was close to that obtained in the preparation of the support ($g\text{-}C_3N_4$, 52.2 %). On the other hand, the iron content in $g\text{-}C_3N_4$ ranged from 2.06 to 5.26 w/w % Fe (Table 1), with greater retention of the metal in the photocatalysts prepared by methods *(i)* to *(iii)*. It would therefore seem that supporting the metallic phase on the previously prepared $g\text{-}C_3N_4$ favors the incorporation of iron. On the other hand, the metal oxides Fe_3O_4 and $\alpha\text{-}Fe_2O_3$ prepared as a reference showed preparation yields of 96 % and the iron contents were very close to the theoretical values (72.42 % Fe and 67.44 % Fe, respectively). The CHN elemental analysis of the solids showed that when the Fe phases were supported on the $g\text{-}C_3N_4$, the carbon (maximum of 5 %) and nitrogen (maximum 10 %) contents decreased. In the solids $Fe^{n+}/g\text{-}C_3N_4$ and $\alpha\text{-}Fe_2O_3/g\text{-}C_3N_4$ the decrease in the content of C and especially N was more significant than with $g\text{-}C_3N_4$, which may be related to the reducing and oxidizing atmospheres, respectively, used during their final calcinations. When carbon nitride was structurally doped with iron (method *iv*), there was a negligible decrease in the contents of these elements. However, the hydrogen content increased slightly, reaching a value close to 2.50 % for all photocatalysts. It is important to clarify that the C/N ratio for all materials remained unchanged (~0.51). The sum of the weight percentages of C, H and N and the iron content had a value close to 100 % only for the $g\text{-}C_3N_4$ and Fe-$g\text{-}C_3N_4$ materials. In contrast, for the three supported photocatalysts, the sum was lower, suggesting that the iron supported in these materials was stabilized in an oxidized state at different levels, even for the solid $Fe^{n+}/g\text{-}C_3N_4$, despite having been calcined in a reducing atmosphere.

The XRD patterns of the powder materials were analyzed to investigate the structure and crystallinity of the photocatalysts and support (Fig. 1). In the $g\text{-}C_3N_4$ support and in all the prepared photocatalysts, two pronounced diffraction peaks were observed mainly around 13.2 °2θ and 27.4 °2θ, assigned to the 100 and 002 planes of the $g\text{-}C_3N_4$ phase, with a hexagonal structure (space group P-6 m2) that corresponds to the structural packing in the tri-*s*-triazine plane of $g\text{-}C_3N_4$ and the interplanar distance between the C_3N_4 sheets, respectively [7,25]. Furthermore, the conjugated aromatic structure for all materials has a distance of d_{002} between sheets of approximately 3.25 Å (Table 2), which is characteristic of carbon nitrides [52]. This demonstrates that the graphitic C_3N_4 structure was formed with a negligible presence of organic impurities in the semiconductor support.

However, the intensity of the 100 and 002 diffraction peaks clearly decreases in the photocatalysts prepared by methodologies *(i)* to *(iii)* where different iron phases were supported ($Fe^{n+}/g\text{-}C_3N_4$, $Fe_3O_4/g\text{-}C_3N_4$ and $\alpha\text{-}Fe_2O_3/g\text{-}C_3N_4$), affecting to a large extent the crystallinity of the semiconductor phase (Fig. 1). In contrast, for the Fe-$g\text{-}C_3N_4$ photocatalyst, the intensity of the signals was better maintained, suggesting that the Fe species were chemically coordinated with the nitrogen atoms of the aromatic rings of tri-*s*-triazine, probably forming Fe-N bonds, as mentioned by other researchers [26,53]. The above is consistent with the full width half maximum (FWHM) in plane 002 (Table 2), where the Fe-$g\text{-}C_3N_4$ material (1.52 °2Θ) presented a narrower value than that of the other photocatalysts, $Fe^{n+}/g\text{-}C_3N_4$ (1.63 °2Θ), $Fe_3O_4/g\text{-}C_3N_4$ (1.59 °2Θ), and $\alpha\text{-}Fe_2O_3/g\text{-}C_3N_4$ (1.60 °2Θ), and a value almost equal to that of $g\text{-}C_3N_4$ (1.51 °2Θ), indicating that the lamellar structure was preserved [18]. Additionally, the (1 0 0) diffraction plane for Fe-$g\text{-}C_3N_4$ showed a wide signal (FWHM = 2.64 °2Θ) with lower intensity than the other photocatalysts (Table 2), suggesting a greater proportion of Fe species doping the layered structure of the semiconductor [53]. On the other hand, for the $Fe^{n+}/g\text{-}C_3N_4$ solid, the signal in the 100 plane was affected to a lesser extent with a FWHM of 1.87 °2Θ. This could indicate that preparing the materials in an H_2 atmosphere largely avoided the formation of larger iron oxide particles and that part of the Fe^{n+} (n = 2 or 3) was probably interlayered between the sheets of $g\text{-}C_3N_4$, significantly affecting the crystallinity in this plane.

In addition to the above, characteristic signals of iron oxides were not observed in the Fe-$g\text{-}C_3N_4$ and $Fe^{n+}/g\text{-}C_3N_4$ photocatalysts. In contrast, in $Fe_3O_4/g\text{-}C_3N_4$ and $\alpha\text{-}Fe_2O_3/g\text{-}C_3N_4$ there were diffraction peaks that agreed with those observed for the prepared pure magnetite and pure hematite (Fig. S1) which also coincide with peaks reported in the literature [28,41]. The signals correspond well with the (2 2 0), (3 1 1), (4 0 0), (4 2 2), (5 1 1) and (4 4 0) diffraction planes of the cubic crystal structure centered on the faces of pure Fe_3O_4 (space group: Fd3m), and the diffraction planes (0 1 2), (1 0 4), (1 1 0), (1 1 3), (0 2 4), (1 1 6), (0 1 8), (2 1 4) and (3 0 0) for the rhombohedral structure of pure $\alpha\text{-}Fe_2O_3$ (space group: R-3C) [54]. Such two photocatalysts did not show change in the crystalline phase of the iron oxides after being supported. However, a slight increase in the crystallite size was observed for the Fe_3O_4 phase from 10.19 nm to 12.62 nm in $Fe_3O_4/g\text{-}C_3N_4$ and a decrease for the $\alpha\text{-}Fe_2O_3$ phase from 21.61 nm to 14.75 nm in $\alpha\text{-}Fe_2O_3/g\text{-}C_3N_4$, in comparison with the reference mass oxide phases.

The FTIR spectra (Fig. 2) showed strong bands in the region from 1200 to 1700 cm^{-1} characteristic of the C-N and C=N bond tension in the heterocyclic structure of $g\text{-}C_3N_4$ [18,36]. Additionally, strong bands at 810 cm^{-1} and 883 cm^{-1} were conserved, attributed to the stretching vibrations of the tri-*s*-triazine ring and to the N-H deformation of the amino groups, respectively [36]. Finally, a broad signal can be observed between 3100 and 3500 cm^{-1} associated with the vibrations of NH and NH_2 groups that could be generated in incomplete polymerizations or through vibrations of the -OH group due to physisorbed water [36]. The Fe-$g\text{-}C_3N_4$ material was the only photocatalyst that did not present characteristic bands of Fe–O oxides in the 450 and 550 cm^{-1}region, in strong agreement with what was observed by the XRD analysis. The supported oxides $Fe_3O_4/g\text{-}C_3N_4$ and $\alpha\text{-}Fe_2O_3/g\text{-}C_3N_4$ presented vibration bands similar to those of their pure oxides (Fig. S2), but of lower intensity. It is important to highlight that $Fe^{n+}/g\text{-}C_3N_4$ presented a vibration between 500 and 650 cm^{-1}, similar to that observed in $Fe_3O_4/g\text{-}C_3N_4$, inferring that calcination in a reducing atmosphere did not guarantee that the metal was stabilized in elemental form, and instead small oxide particles were generated with very small crystallite sizes,

Table 1
Elemental composition and yield in the preparation of photocatalysts, graphitic carbon nitride and reference oxides (dry basis).

Sample	Elemental composition[a] (w/w %)			[Fe][b] (w/w %)	Yield (%)
	C content	H content	N content		
$g\text{-}C_3N_4$	33.45	2.38	64.17	NA	52.2
Fe-$g\text{-}C_3N_4$	32.81	2.50	62.70	2.06	49.5
$Fe^{n+}/g\text{-}C_3N_4$	27.91	2.51	54.27	5.26	28.5
$Fe_3O_4/g\text{-}C_3N_4$	30.67	2.49	59.74	4.56	51.9
$\alpha\text{-}Fe_2O_3/g\text{-}C_3N_4$	27.92	2.47	54.73	4.45	44.2
Fe_3O_4	NA	NA	NA	72.42	96.5
$\alpha\text{-}Fe_2O_3$	NA	NA	NA	67.44	96.0

[a] Determined by CHN elemental analysis of the solids;
[b] Determined by AAS; NA: not applicable.

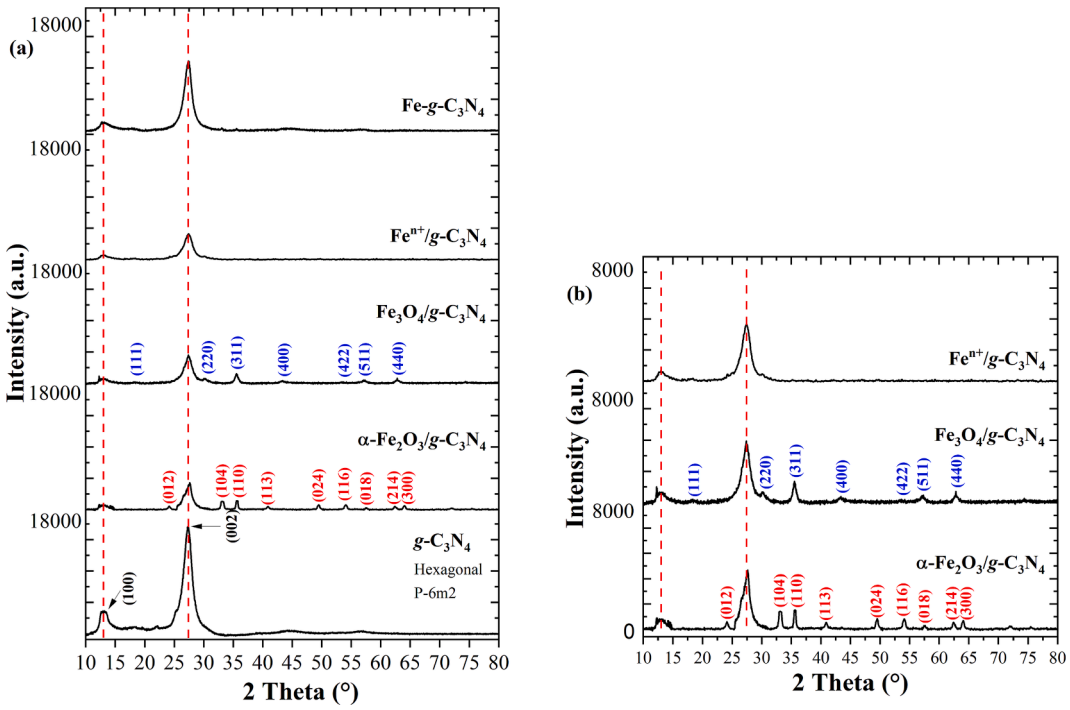

Fig. 1. Powder XRD patterns of graphitic carbon nitride and photocatalysts as compared with reference oxides (α-Fe_2O_3 in red, Fe_3O_4 in blue): (a) full comparison; (b) zoomed XRD patterns of the supported photocatalysts. (For interpretation of the references to colour in this figure legend, the reader is referred to the web version of this article.)

Table 2
Physicochemical properties of photocatalysts, graphitic carbon nitride and reference oxides (dry basis).

Sample	d_{002} (Å)	$FWHM_{002}$ (° θ)	$FWHM_{100}$ (° θ)	Bandgap (eV)[a]	D[b] (nm)	S_{BET} (m^2/g)	S_{ext} (m^2/g)	Pore volume[c] (cm^3/g)
g-C_3N_4	3.25	1.51	1.61	2.86	NA	31	29	0.12
Fe-g-C_3N_4	3.26	1.52	2.64	2.80	NA	9	8	0.03
Fe^{n+}/g-C_3N_4	3.25	1.63	1.87	2.81	NA	31	29	0.13
Fe_3O_4/g-C_3N_4	3.24	1.59	1.62	2.83	12.6	51	46	0.27
α-Fe_2O_3/g-C_3N_4	3.24	1.60	1.63	2.84	14.7	29	27	0.13
Fe_3O_4	NA	NA	NA	1.78	10.2	112	112	0.31
α-Fe_2O_3	NA	NA	NA	2.04	21.6	39	37	0.31

[a] Determined by DR UV–Vis;
[b] D: average size of crystallite calculated from the XRD signal (002) by the Scherrer equation, for Fe_3O_4 from signal (311) and for α-Fe_2O_3 from signal (104);
[c] Determined by BJH analysis over the desorption branch, from the N_2 adsorbed at $p/p^0 \geq 0.95$; *FWHM*: full width at half maximum; S_{BET}: BET specific surface; S_{ext}: external surface from the *t-plot*; NA: not applicable.

which could not be observed by XRD analysis.

The textural properties of the g-C_3N_4 starting material and the photocatalysts were estimated from type IV adsorption/desorption isotherms with type H3 hysteresis (Fig. 3), characteristic of mesoporous materials and structures with slit-shaped pore morphology [25], formed from sheets of non-uniform shape and/or size [18].

The specific surface area (S_{BET}) for all photocatalysts was mainly represented by their external surface area (S_{ext}) (Table 2). It is important to highlight that the specific surface area of the Fe^{n+}/ y α-Fe_2O_3/ iron phases supported on g-C_3N_4, was conserved, while for Fe_3O_4/g-C_3N_4 it increased due to the incorporation of the magnetite phase which generated an increase in the pore volume (cm^3/g). On the other hand, the photocatalyst prepared by doping it with iron (Fe-g-C_3N_4), had a notable decrease in the S_{BET} (9 m^2/g). This suggests that doping with Fe significantly obstructed the porosity, as also evidenced by the substantial decrease in the pore volume (Fig. 3). However, the type of porosity remained unchanged, correlating properly with the results found by the XRD analyses concerning the (1 0 0) diffraction planes. According to recent reports [7,55], such incorporation of iron species into the crystalline structure of the graphitic carbon nitride takes place by coordination with the nitrogen atoms of the tri-*s*-triazine aromatic ring, which disturb the regular arrangement of the carbon and nitrogen atoms without appreciable changes in the morphology of the particles, but affecting the porosity of the material, which in turn contributes to reducing its specific surface.

Using the DR UV–visible spectra, the light absorption range of the photocatalysts was determined by looking at the bandgap value (Table 2), which is especially important for the photodegradation of organic pollutants. The graphitic carbon nitride support (g-C_3N_4) showed a bandgap of 2.86 eV corresponding to a λ of maximum absorption of 434 nm, which means that it exhibits photocatalytic activity under visible light radiation [28,56]. For all photocatalysts, the band gap decreased slightly, increasing the proportion of visible light to the same degree, suggesting that the change altered the electronic structure and improved light absorption. There was a clear change in the bandgap for the Fe-g-C_3N_4 and Fe^{n+}/g-C_3N_4 photocatalysts, reaching values of 2.80 eV (λ = 443 nm) and 2.81 eV (λ = 441 nm). On the other hand, the stabilization of the iron oxide particles improved when they were supported on g-C_3N_4 since they seem to have promoted more photo-induced electron pairs under visible light irradiation [56] than those obtained by

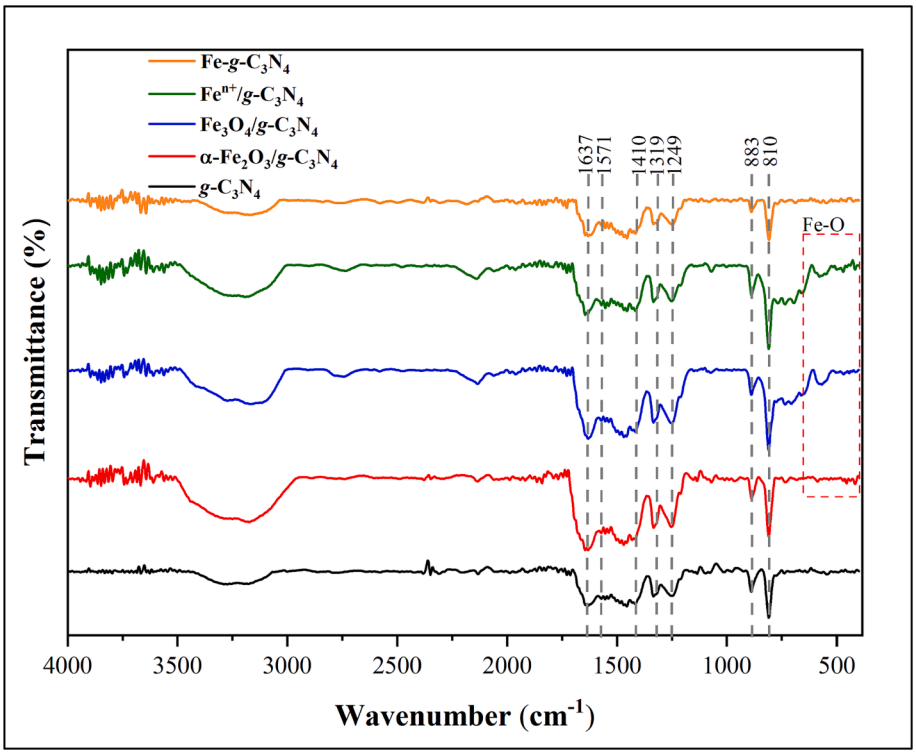

Fig. 2. IR spectra of graphitic carbon nitride and photocatalysts.

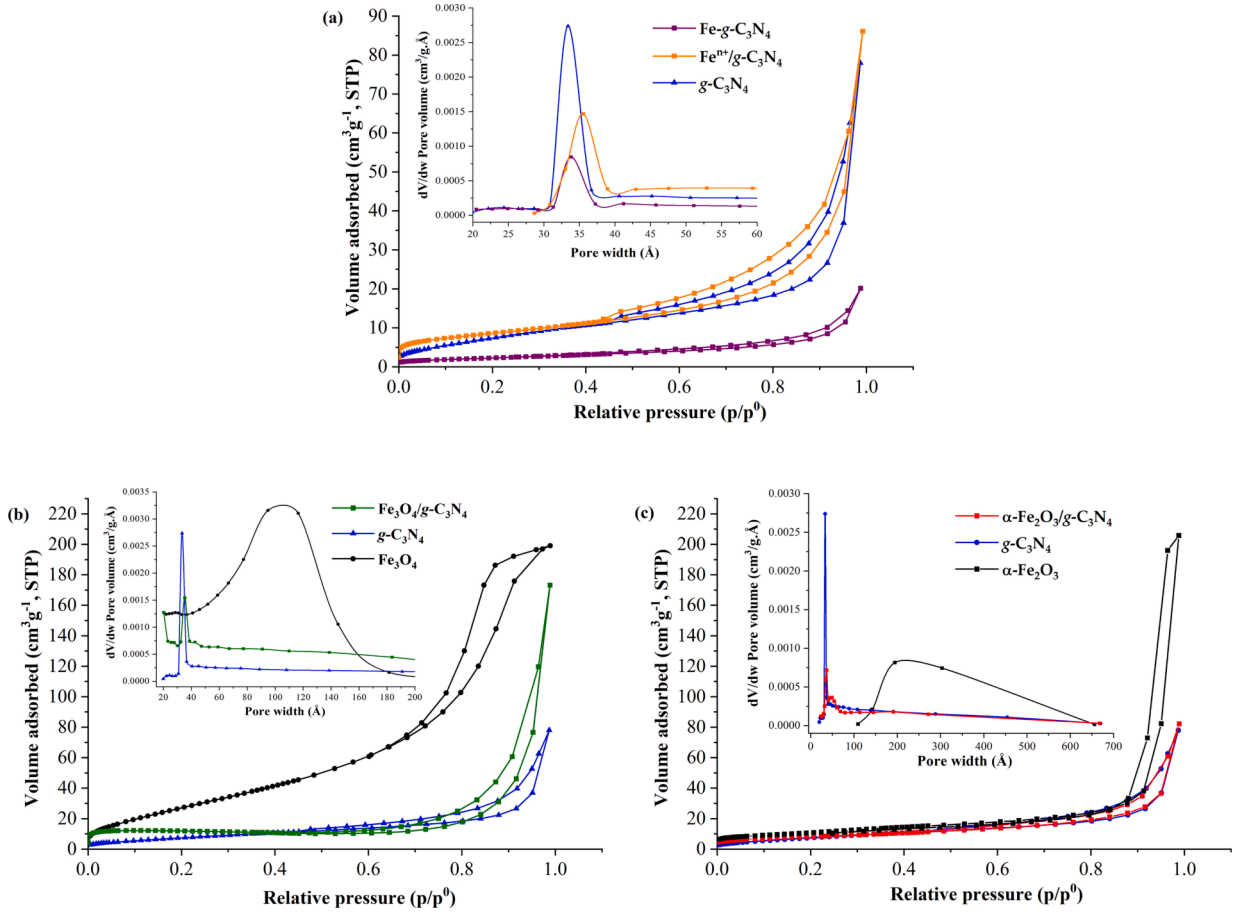

Fig. 3. N_2 adsorption–desorption isotherms and pore-width distributions of the photocatalysts at 77 K: (a) Fe-g-C_3N_4, and Fe^{n+}/g-C_3N_4, (b) Fe_3O_4/g-C_3N_4 and (c) α-Fe_2O_3/g-C_3N_4.

their pure oxides.

The thermogravimetric analysis of the materials (Fig. 4) showed resistance of the support to decomposition up to temperatures of 550 °C and 620 °C in air and nitrogen atmospheres, respectively. In contrast, the stability of all photocatalysts in air atmosphere decreased to values close to 440 °C (Fig. 4 and Fig. S3). This suggests that close contact was established between the iron and iron oxides and the semiconductor support, causing a decrease in the stability of their C-N bonds [28]. In the nitrogen atmosphere, the photocatalysts were stable up to 550 °C for Fe-*g*-C_3N_4 and 500 °C for the supported photocatalysts (Fig. S3). In other words, the Fe-doped material maintained a thermogram practically identical to that of *g*-C_3N_4 in a N_2 atmosphere, and the thermal stability only slightly decreased in the supported Fe oxides.

For all the prepared materials, the H_2 reduction curves at a temperature programmed (Fig. 5) showed a reduction event at 677 °C for *g*-C_3N_4 that can be attributed to the decomposition of the support. As observed in TGA analysis in inert atmosphere, *g*-C_3N_4 sublimes and C-N bonds are completely destroyed between 600 °C and 700 °C. All photocatalysts exhibited a single reduction event which completely overlapped with the decomposition signal of graphitic carbon nitride. The total consumption of experimental H_2 per gram of material to completely reduce the iron and iron oxides in each photocatalyst (Table 3) was very close to the theoretical values (Table 1). On the other hand, it was observed that the complete reduction of iron in an inert atmosphere occurred at lower temperatures (~620 °C – 630 °C) for the supported photocatalysts (Fe^{n+}/*g*-C_3N_4, Fe_3O_4/*g*-C_3N_4 and α-Fe_2O_3/*g*-C_3N_4) than for the support (Fig. S3). The Fe^{n+}/*g*-C_3N_4 photocatalyst exhibited a small shoulder at approximately 531 °C. This could be attributed to iron oxide particles in their Fe_3O_4 phase that, during calcination in a H_2 atmosphere in their preparation, were able to form with a crystallite size so small that they could not be identified by XRD analysis. This complements the assumption made when analyzing the X-ray diffraction pattern for the Fe^{n+}/*g*-C_3N_4 photocatalyst. It is also important to mention that the iron-doped photocatalyst (Fe-*g*-C_3N_4) exhibited a reduction temperature slightly higher than that of the support (687 °C), revealing that there is a notable difference in the location of the active metal in the structure of the photocatalyst, between the Fe-*g*-C_3N_4 and Fe^{n+}/*g*-C_3N_4 materials.

The pure iron oxide magnetite (Fig. 5) experienced two reduction events that corresponded to the gradual reduction of the oxides to elemental iron ($Fe_3O_4 \rightarrow FeO \rightarrow Fe^0$). These events overlap slightly. The reduction of the iron phase from Fe_3O_4 to FeO occurred at 587 °C and the subsequent reduction of FeO to Fe^0 occurred at 715 °C [57]. There were three reduction events for hematite ($Fe_2O_3 \rightarrow Fe_3O_4 \rightarrow FeO \rightarrow Fe^0$). The first was a narrow reduction event, with a maximum temperature of 324 °C that can be attributed to the reduction of α-$Fe_2O_3 \rightarrow Fe_3O_4$ [58]. The other two events correspond to the gradual reductions of Fe_3O_4 [59]. There was a slightly lower total hydrogen consumption for magnetite (17,372 μmol H_2/g) than for hematite (18,091 μmol H_2/g).

Additionally, in order to further explore the state of the iron in the graphitic carbon nitride modified by each method, the photocatalysts were analyzed by X-ray photoelectron spectroscopy (XPS). The general spectrum (Fig. 6) of the *g*-C_3N_4 support shows peaks characteristic of carbon (C_{1s}) at 283 eV, nitrogen (N_{1s}) at 392 eV and oxygen (O_{1s}) at 528 eV. The presence of oxygen in the *g*-C_3N_4 and Fe-*g*-C_3N_4 materials may be due to O_2 or H_2O adsorbed onto the surface [29]. When the support was modified with the different iron phases, an additional signal could be seen at 709 eV corresponding to the binding energy of iron (Fe2p). The intensity of this signal is directly correlated with the iron concentration determined by AAS. The high-resolution spectra are presented in Fig. 7. For *g*-C_3N_4, the XPS spectrum of C_{1s} (Fig. 7(a)) can be deconvoluted into two peaks with binding energies of 283.9 eV and 287.2 eV which can be assigned to the sp^2 hybridized carbon (C = C) and carbon bonds of the nitride heptazine structure (N-C = N), respectively [7,29]. These signals are very well defined in all the prepared photocatalysts. Strikingly, an additional signal was observed at a binding energy higher than 287 eV in the photocatalysts Fe^{n+}/*g*-C_3N_4, Fe_3O_4/*g*-C_3N_4 and α-Fe_2O_3/*g*-C_3N_4, which can be associated to C-O and C=O [60], thanks to the oxygen most likely coming from the iron oxides. It should be noted that the modification with the metal brought a small variation in the bond energy with respect to *g*-C_3N_4 for the materials in which the metal oxides were supported, since the bond energies increased slightly, while for Fe-*g*-C_3N_4 they decreased. This may be due to the incorporation of iron in *g*-C_3N_4, the carbon nitride structure, rather than on the surface of

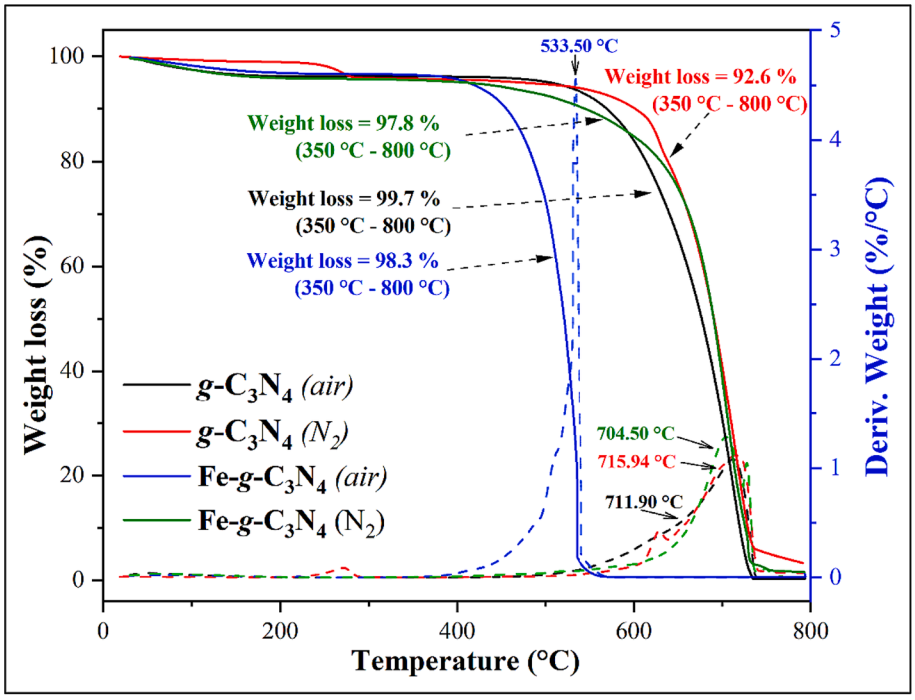

Fig. 4. TGA diagrams of the *g*-C_3N_4 support and the photocatalyst Fe-*g*-C_3N_4 under either N_2 or air atmospheres: full lines represent weight loss; dotted lines represent first derivative of the weight loss.

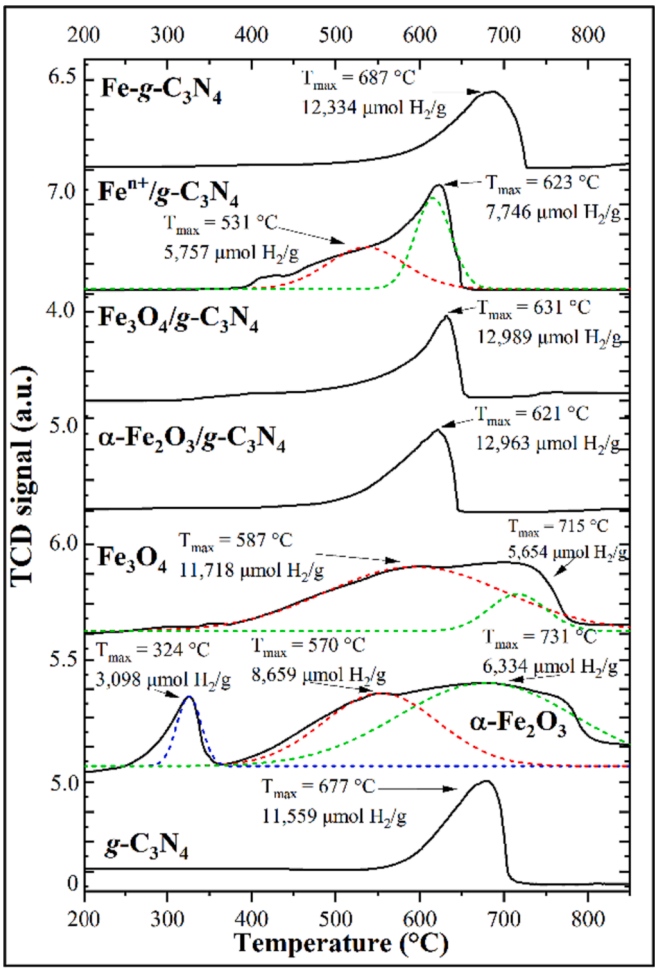

Fig. 5. H_2-TPR thermal diagrams of g-C_3N_4, photocatalysts and reference oxides.

Table 3
Total hydrogen consumption by the semiconducting support and the photocatalysts through the Temperature Programmed Reduction (H_2-TPR).

Sample	H_2 consumption (µmol/g)		
	Measured[a]	Expected[b]	Expected from the Fe content[c]
g-C_3N_4	11,559	NA	11,559
Fe-g-C_3N_4	12,334	552	12,111
Fe^{n+}/g-C_3N_4	13,503	1,490	13,049
Fe_3O_4/g-C_3N_4	12,989	1,086	12,645
α-Fe_2O_3/g-C_3N_4	12,963	1,192	12,751
Fe_3O_4	17,372	17,243	17,243
α-Fe_2O_3	18,091	18,064	18,064

[a] Experimental consumption in the range 200–800 °C;
[b] Theoretical expected consumption from the stoichiometric reduction of the measured Fe content (AAS): for Fe^{n+}/g-C_3N_4, Fe_3O_4/g-C_3N_4, and Fe_3O_4, magnetite distribution of oxidation states in Fe is assumed, whereas full iron content is assumed to be Fe^{3+} in the other samples;
[c] Theoretical expected consumption from the Fe content plus the experimental consumption of g-C_3N_4.

the semiconductor. The XPS spectrum of N_{1s} (Fig. 7(b)) for g-C_3N_4 can be split into three subpeaks at 395.8 eV, 397.6 eV and 399.3 eV. These can be assigned to the nitrogen atoms with sp^2 bonds in the triazine rings (C-N=C), to the presence of the N-$(C)_3$ or H-N-$(C)_2$ bonds and to the $-NH_2$ or =NH groups, respectively [29]. Compared to the C_{1s} spectrum, the N_{1s} peaks were slightly shifted towards higher energies, especially for the Fe-g-C_3N_4 photocatalyst, suggesting that the Fe^{3+} ions bind to the

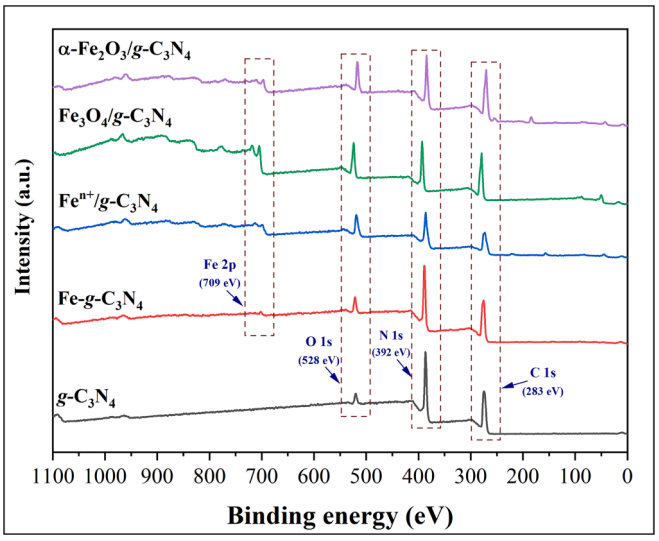

Fig. 6. General XPS spectra of g-C_3N_4 and the photocatalysts.

lattice atoms of nitrogen rather than to the carbon atoms.

The XPS spectrum of O_{1s} (Fig. 7(c)) for g-C_3N_4 and Fe-g-C_3N_4 revealed a single signal with a binding energy of 530.9 eV and 530.5 eV respectively, attributed to water adsorbed on the surface. However, for the other photocatalysts, two signals were observed, one at approximately 531.0 eV and another at 528.7 eV, which confirms the presence of Fe-O-Fe and Fe-OH bonds in these materials [30]. The above confirms what was suggested by the XRD diffractograms, establishing that through preparation methodology *(iv)*, for Fe-g-C_3N_4 it was effectively possible to incorporate iron into the g-C_3N_4 structure due to the absence of the characteristic Fe-O bond signal. The same can be said for Fe^{n+}/g-C_3N_4, where signals were not observed in XRD, but they were in XPS. It can therefore be established that the preparation in an H_2 atmosphere did not favor the stability of the metal in the elemental state, but rather in Fe^{n+}/g-C_3N_4 it led to the formation of highly dispersed particles very similar to that of supported Fe_3O_4 (Fig. 7(d)).

Finally, in the XPS Fe_{2p} spectrum (Fig. 7(d)), for all photocatalysts there were two main peaks between 709 eV and 730 eV, which correspond to the high-spin multiplet $Fe_{2p1/2}$ and $Fe_{2p3/2}$. In the Fe^{n+}/g-C_3N_4 and Fe_3O_4/g-C_3N_4 photocatalysts, binding energies at 711.1 eV and 724.3 eV were observed, characteristic of the presence of iron in the form of magnetite. In other words, there were two oxidation states: Fe^{2+} (711 eV) and Fe^{3+} (715 eV) [60]. This suggests that for Fe^{n+}/g-C_3N_4, the metal was most likely stabilized when oxidized in the magnetite phase, as stated before. On the other hand, in Fe-g-C_3N_4 and α-Fe_2O_3/g-C_3N_4 the binding energies were approximately 715 eV and 729 eV. This indicates the presence of iron in its oxidation state (3+) only, the difference being that the iron in Fe-g-C_3N_4 is stabilized in the structure through coordinated Fe-N bonds, as emerged from the analysis of the high-resolution N_{1s} spectra, while in α-Fe_2O_3/g-C_3N_4 the iron oxide was apparently stabilized by interacting at the same time with the N and C atoms of g-C_3N_4. The combined analyses by X-ray diffraction, X-ray photoelectron spectroscopy, and H_2 - temperature programmed reduction, were also consistent with some recent reports trying to understand the high redox reactivity of Fe-doped-g-C_3N_4 materials by means of DFT calculations [61–63]. Furthermore, based on this background and the methodology of similar, though not identical, synthesis methods reported by some authors [7,18,26], it is very likely that the coordination structure of the active sites stabilized in the photocatalyst Fe-g-C_3N_4 to be of the type Fe-N_6 [63].

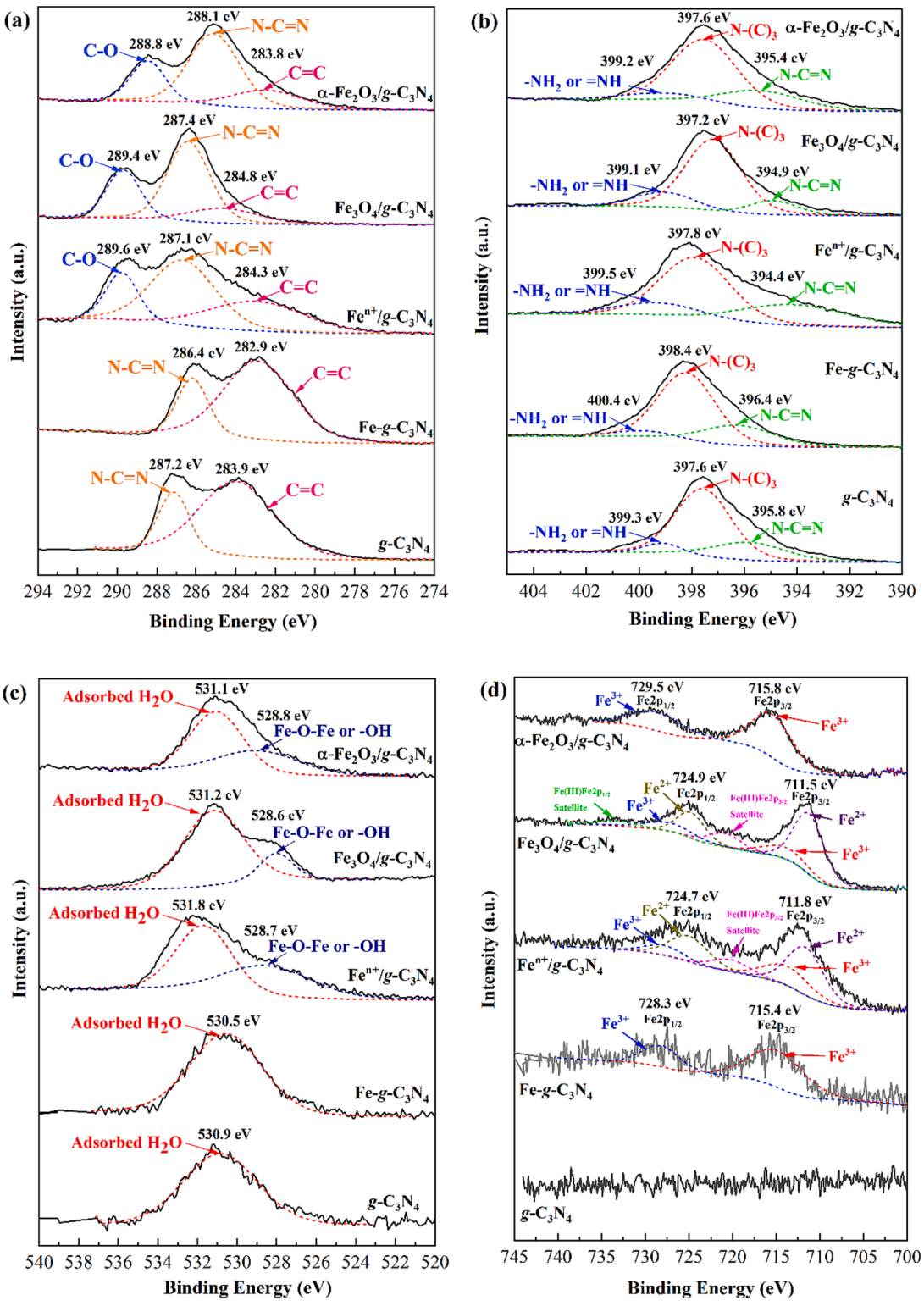

Fig. 7. High-resolution XPS spectra of g-C_3N_4 and the photocatalysts: (a) C_{1s}, (b) N_{1s}, (c) O_{1s} and (d) Fe_{2p}.

3.2. Evaluation of photocatalysts in the degradation of phenol

Fig. 8 compares the evolution of the degradation and concentration of dissolved organic carbon in phenol solutions through the photo-assisted heterogeneous Fenton reaction, in the presence of a set of g-C_3N_4 photocatalysts modified with iron phases at neutral initial pH. It should be noted that Fe^{n+}/g-C_3N_4 and Fe-g-C_3N_4 exhibited close to 100 % phenol degradation in only 45 min of reaction, with maximum mineralization of 77 % and 64 %, respectively (Table 4), in 3 h of reaction. However, Fe^{n+}/g-C_3N_4 showed a much higher concentration of dissolved Fe than that of Fe-g-C_3N_4, suggesting that its catalytic response significantly followed homogeneous Fenton activation. On the other hand, although the iron-oxide-supported photocatalysts exhibited leached Fe concentrations lower than 0.018 mg Fe/L, their efficiency at both degrading phenol and mineralizing DOC was clearly lower. According to very recent reports [62,63], the combined photocatalytic-

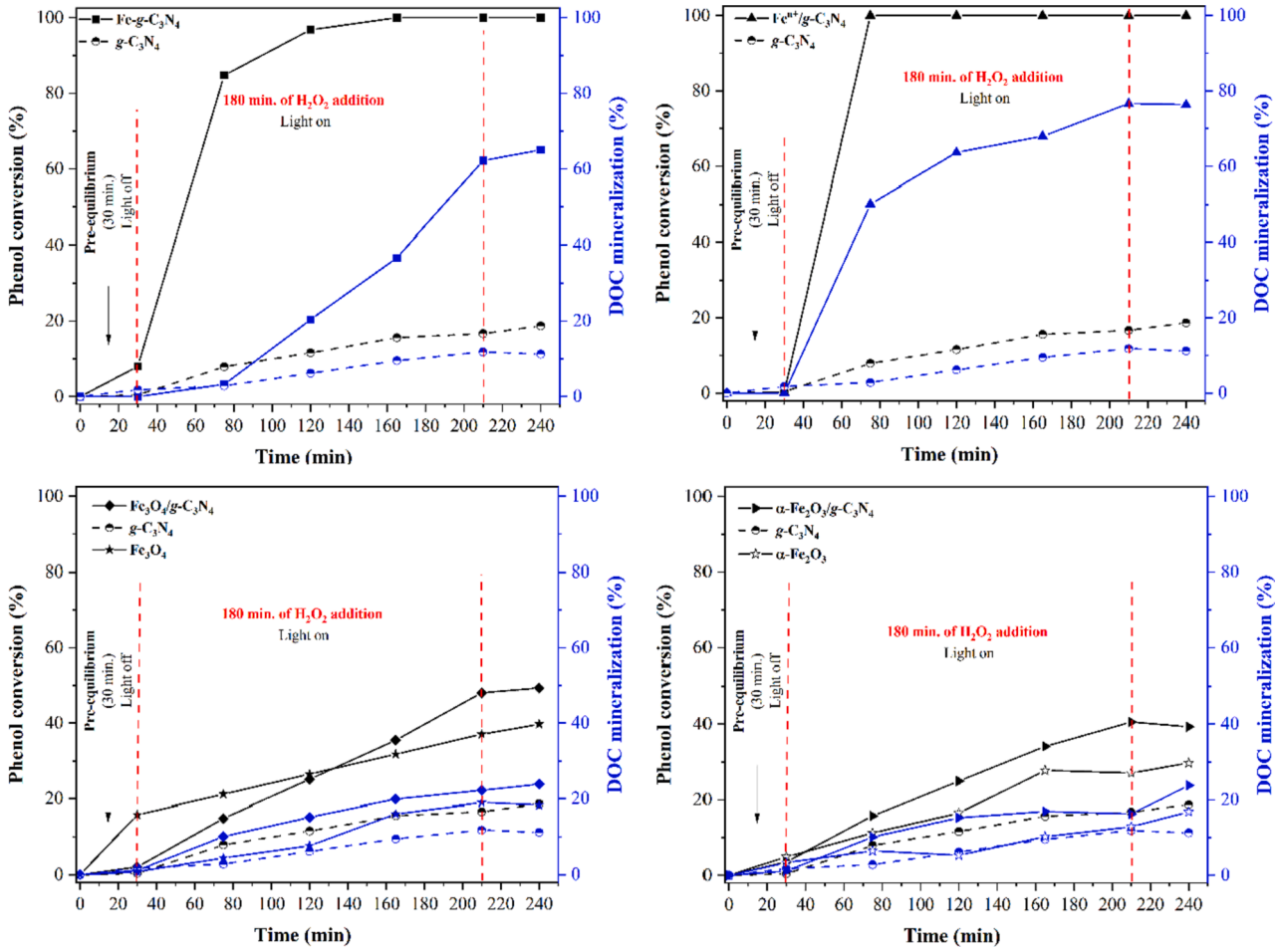

Fig. 8. (Photo)-catalytic response of the materials in the heterogeneous Fenton degradation of phenol (PhO) under visible-light irradiation: $[Fe_{cat}]$ = 50 mg/L; $[PhO]_0$ = 13.07 mg/L (10.0 mg DOC/L); $[H_2O_2]_{add.}$ = 11.34 mmol/L, $V_{add}.H_2O_2$ = 60 mL; pH_0 = 7.0; irradiation power = 70 W; T = 25.0 ± 0.2 °C.

Table 4
Photocatalytic performance of the iron-modified g-C_3N_4 solids in the degradation of phenol (PhO) at circumneutral pH under visible-light irradiation.

(photo)-catalytic test	PhO degradation[a] (%)	DOC mineralization[b] (%)	$(H_2O_2)_{reacted}$[c] (%)	$[Fe]_{leached}$[d] (mg/L)
g-C_3N_4	18	11	19	0.000
Fe-g-C_3N_4	100	64	78	0.013
Fe^{n+}/g-C_3N_4	100	77	92	1.490
Fe_3O_4/g-C_3N_4	48	24	58	0.016
α-Fe_2O_3/g-C_3N_4	41	18	52	0.018
Fe_3O_4	40	18	48	0.467
α-Fe_2O_3	30	17	39	0.312
g-C_3N_4 dark	10	7	10	0.000
Fe-g-C_3N_4 Fenton	99	17	27	0.013
Fe-g-C_3N_4 Photocat.	25	3	NA	0.012
Fe-g-C_3N_4 Ads.	5	2	NA	0.010
H_2O_2 + light blank	14	9	100	NA
Light	10	2	NA	NA
Fe-g-C_3N_4 pH 3.0	100	100	100	0.094

[a] Determined by HPLC-PDA at 270 nm;
[b] Determined by TOC analysis of the 0.45 μm – filtered samples;
[c] Determined by colorimetric analysis at λ_{max} = 444 nm;
[d] Determined by AAS; $(H_2O_2)_{reacted}$ = reacted fraction of H_2O_2; $[Fe]_{leached}$ = Fe concentration in the reaction's effluent measured by AAS; t of reaction: 3 h. NA = not applicable.

Fenton performance exhibited by this kind of solids is strongly ruled by the efficiency of the photoelectron transfer from the g-C_3N_4 photoactive phase onto the Fe-active sites; this phenomenon seems largely facilitated by the high-electron density occurring on the Fe-N bonds in this type of metal-doped semiconducting phases, as in the case of the Fe-g-C_3N_4 material. Thus, in Fe-g-C_3N_4 the photoinduced electronic charge can promptly migrate from g-C_3N_4 onto (Fe^{3+}-Nx) sites here revealed, subsequently being quickly reduced into Fe^{2+} promoting the faster Fenton activation of H_2O_2 [7,61–63]; this of course accompanied by a faster generation of reactive oxidizing species, and eventually translated in better phenol and DOC degradation efficiencies as observed (Fig. 8). In contrast, the electron density on the metal sites in the supported oxides

like Fe_3O_4/g-C_3N_4 and α-Fe_2O_3/g-C_3N_4 may decrease due to the crystalline aggregates of iron oxides formed [63].

Fig. 9 shows the catalytic response of Fe-g-C_3N_4 together with a series of blank experiments. Neither the simple adsorption of phenol and its byproducts (*Fe-g-C_3N_4 Ads.*), which was insignificant, nor the purely photocatalytic reaction (without H_2O_2 addition) from the irradiation of the functionalized semiconductor (*Fe-g-C_3N_4 Photocat.*) explain individually or additively the high degradation of phenol in less than 60 min of reaction, and a DOC mineralization of over 60 % in 3 h of reaction. Instead, comparing the Fe-g-C_3N_4 (with visible-light-irradiation) and Fe-g-C_3N_4 *Fenton* (without irradiation) experiments revealed that the efficiency of Fenton degradation significantly increases in the presence of visible-light irradiation, especially DOC mineralization which triples when irradiated. This increase was accompanied by a significant increase in the fraction of reacted H_2O_2, which went from 27 % to 78 %. Simple irradiation of the contaminated solution, with or without the presence of H_2O_2, also did not explain the outstanding catalytic performance of the Fe-functionalized semiconductor phase (Fig. S4). The catalytic results demonstrated that the structurally doped Fe in g-C_3N_4 notably increases its reactivity in the heterogeneous photo-Fenton reaction in the presence of visible light, even in conditions of circumneutral pH. This could be attributed to the fact that the photoelectrons excited to the conduction band of semiconductor can accelerate the reduction of Fe^{3+} into Fe^{2+}, the kinetically slowest stage of the Fenton mechanism, as has been widely reported in the literature [7,27]. It is then possible claiming that the activity of the Fe-g-C_3N_4 catalyst was significantly improved through the synergistic effect between photocatalysis and the Fenton reactions, similar to others investigations made in the presence of other contaminants or under different reaction conditions [7,55,61,63,64], where the process has been called in dissimilar ways such as “heterogeneous photocatalysis-Fenton” or “photo-Fenton-like” processes.

It is remarkable that decreasing the pH to 3.0 (Fe-g-C_3N_4 pH 3.0, Fig. S4), the optimal pH where the Fenton process operates most efficiently (2.4–3.4) [65], resulted in a large increase in the degradation and mineralization rate of the contaminant and the reaction byproducts compared to the response at circumneutral pH. While the differences in terms of phenol degradation are not as impressive, with 120 min of reaction achieving a degradation of 96 % under both conditions, the mineralization of DOC after 4.0 h of reaction at pH 3.0 reached 100 %, which is very rarely observed even in conventional homogeneous Fenton processes.

Finally, reusability is a crucial parameter in the practical application of the Fenton solid catalysts. Therefore, the photocatalyst with the best performance was used for five sequential cycles in the visible-light-assisted heterogeneous Fenton degradation of phenol (Fig. 10). After five cycles in the presence of the Fe-g-C_3N_4, there was a reduction of approximately 19 % and 24 % in the phenol conversion and the DOC mineralization, respectively. This reduction can be attributed in part to the Fe leaching during the reuse cycles R1 (0.010 mg Fe/L) and R2 (0.004 mg Fe/L), but after that the metal was remarkably stable since dissolved Fe was below the LOD of the AAS equipment (0.0034 mg/L). According to previous reports, such a decrease in the (photo)-catalytic performance could be typically ascribed to iron complexing with phenol degradation by-products [66], mainly catechol and oxalic acid whose hydroxyl and carboxylic functional groups [67–69], are sufficiently strong ligands at pH values around 6.0 [70] to stablish competition against the tri-*s*-triazine -Nx chelating groups. However, to realize the intricacy of the visible-light photo-assisted Fenton degradation process and the reusability of this functional photocatalyst from the third reaction cycle at circumneutral pH, it is advisable to conduct further investigations on the nature and stability of such iron complexes.

4. Conclusions

Photocatalysts based on g-C_3N_4 modified with different iron phases and their performance at degrading phenol was studied at very mild temperature and circumneutral pH. These characteristics are common of most contaminated surface water or wastewater streams. The XRD, FTIR, H_2-TPR, and XPS analyses altogether demonstrated the method of

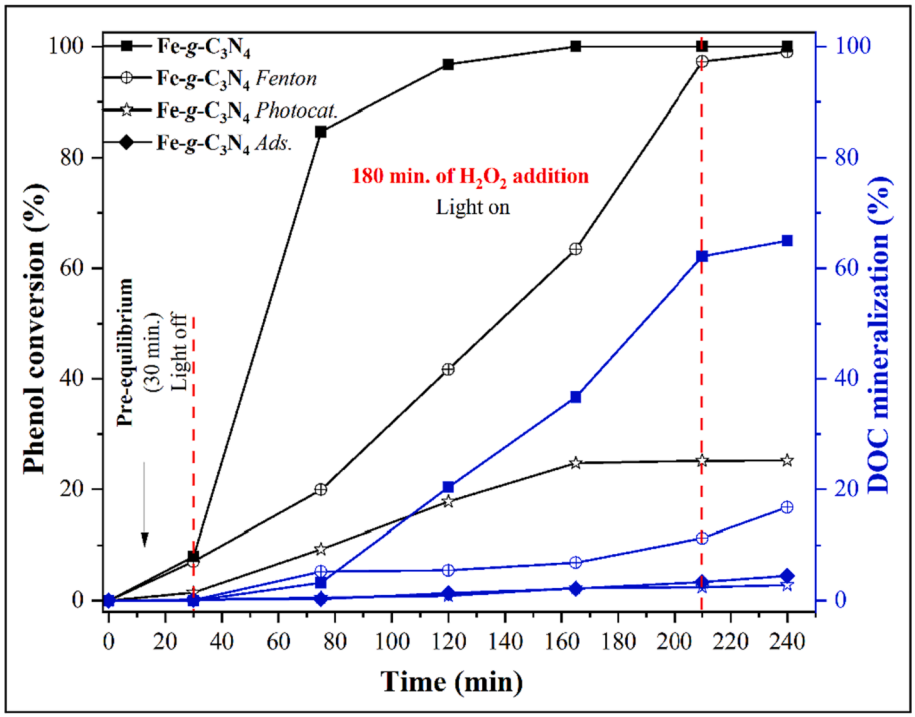

Fig. 9. (Photo)-catalytic response of the materials in the heterogeneous Fenton degradation of phenol (PhO) under visible-light irradiation against blank experiments: $[Fe_{cat}] = 50$ mg/L; $[PhO]_0 = 13.07$ mg/L (10.0 mg DOC/L); $[H_2O_2]_{add.} = 11.34$ mmol/L, $V_{add.}H_2O_2 = 60$ mL; $pH_0 = 7.0$; irradiation power = 70 W; T = 25.0 ± 0.2 °C.

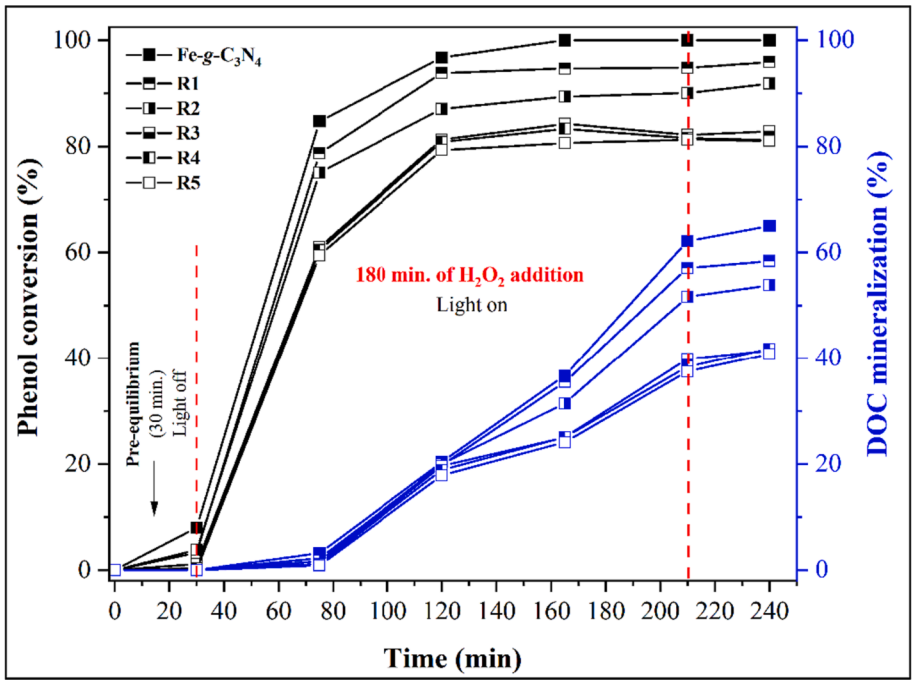

Fig. 10. (Photo)-catalytic response of Fe-*g*-C_3N_4 through five sequential cycles of reuse in the heterogeneous Fenton degradation of phenol (PhO) under visible-light irradiation: $[Fe_{cat}] = 50$ mg/L; $[PhO]_0 = 13.07$ mg/L (10.0 mg DOC/L); $[H_2O_2]_{add.} = 11.34$ mmol/L, $V_{add.}H_2O_2 = 60$ mL; $pH_0 = 7.0$; irradiation power = 70 W; T = 25.0 ± 0.2 °C.

thermal polymerization of the nitride precursors in the presence of Fe to promote the incorporation of the metal as Fe^{3+}, in a very specific location within the framework of the graphitic *g*-C_3N_4, predominantly coordinated by the N atoms of the heptazine rings. The Fe-*g*-C_3N_4 catalyst displayed excellent performance in the heterogeneous Fenton degradation of phenol (85 %, 45 min) photo-assisted with visible light (Xe lamps). It also resulted in an impressive mineralization of dissolved organic carbon (62 %, 180 min) at circumneutral pH, which was higher than that demonstrated by either magnetite or hematite supported on the same substrate or their reference mass oxides. The metal showed to be highly stable even under the stringent oxidizing environment of the photo-assisted Fenton reaction exhibiting insignificant Fe leaching, even throughout five sequential reuse catalytic cycles, degradations and DOC mineralization remaining higher than 80 % and 40 % respectively. Furthermore, the outstanding catalytic performance of this material under unfavorable circumneutral pH was ascribed to a synergistic relationship between visible light-activated photocatalysis and the heterogeneous Fenton process taking place. The results are quite promising in the context of both water purification for drinking water production and tertiary wastewater treatments taking advantage of the solar irradiation.

CRediT authorship contribution statement

Evelyn Alejandra Burbano: Writing – original draft, Investigation. **Carlos Andrés Vallejo:** Writing – original draft, Visualization, Resources, Investigation, Formal analysis, Data curation. **Juan David Ramirez:** Writing – review & editing, Supervision, Project administration, Conceptualization. **Arsenio Hidalgo-Troya:** Writing – review & editing, Validation, Methodology, Formal analysis, Conceptualization. **Luis Alejandro Galeano:** Writing – review & editing, Validation, Resources, Project administration, Methodology, Funding acquisition, Formal analysis, Conceptualization.

Declaration of competing interest

The authors declare that they have no known competing financial interests or personal relationships that could have appeared to influence the work reported in this paper.

Data availability

Data will be made available on request.

Acknowledgement

The funding from *Fondo CTeI* of the *SGR*, Colombia (project BPIN: 2020000100770) is gratefully acknowledged.

Appendix A. Supplementary data

Supplementary data to this article can be found online at https://doi.org/10.1016/j.cej.2024.149766.

References

[1] R.L. Singh, P.K. Singh, Global environmental problems, in: R. Singh (Ed.), Principles and Applications of Environmental Biotechnology for a Sustainable Future. Applied Environmental Science and Engineering for a Sustainable Future, Springer, Singapore, 2017, https://doi.org/10.1007/978-981-10-1866-4_2.
[2] N.A. Khan, V. Vambol, S. Vambol, B. Bolibrukh, M. Sillanpaa, F. Changani, A. Esrafili, M. Yousefi, Hospital effluent guidelines and legislation scenario around the globe: a critical review, J. Environ. Chem. Eng. 9 (2021) 105874, https://doi.org/10.1016/j.jece.2021.105874.
[3] A.S. Qureshi, Challenges and prospects of using treated wastewater to manage water scarcity crises in the Gulf cooperation council (GCC) countries, Water 12 (2020) 1971, https://doi.org/10.3390/w12071971.
[4] N. Morin-Crini, E. Lichtfouse, M. Fourmentin, A.R.L. Ribeiro, C. Noutsopoulos, F. Mapelli, É. Fenyvesi, M.G.A. Vieira, L.A. Picos-Corrales, J.C. Moreno-Piraján, Removal of emerging contaminants from wastewater using advanced treatments. a review, Environ. Chem. Lett. 20 (2022) 1333–1375, https://doi.org/10.1007/s10311-021-01379-5.
[5] R. Rathna, E. Nakkeeran, Phenol degradation from industrial wastewater by engineered microbes, in: S. Varjani, A. Agarwal, E. Gnansounou, B. Gurunathan (Eds.), Bioremediation: Applications for Environmental Protection and

Management. Energy, Environment, and Sustainability, Springer, Singapore, 2018, pp. 1–13, https://doi.org/10.1007/978-981-10-7485-1_13.
[6] P. Chowdhury, S. Nag, A.K. Ray, Degradation of phenolic compounds through UV and visible-light-driven photocatalysis: technical and economic aspects, in: M. Soto-Hernández, M. Palma-Tenango, M. Garcia-Mateos (Eds.), Phenolic Compounds - Natural Sources, Importance and Applications [Internet]. InTech, 2017. https://doi.org/10.5772/66134.
[7] J. Hu, P. Zhang, W. An, L. Liu, Y. Liang, W. Cui, In-situ fe-doped g-C_3N_4 heterogeneous catalyst via photocatalysis-Fenton reaction with enriched photocatalytic performance for removal of complex wastewater, Appl. Catal. B-Environ. 245 (2019) 130–142, https://doi.org/10.1016/j.apcatb.2018.12.029.
[8] S. Jiménez, M. Andreozzi, M.M. Micó, M.G. Álvarez, S. Contreras, Produced water treatment by advanced oxidation processes, Sci. Total Environ. 666 (2019) 12–21, https://doi.org/10.1016/j.scitotenv.2019.02.128.
[9] A. Sharma, J. Ahmad, S. Flora, Application of advanced oxidation processes and toxicity assessment of transformation products, Environ. Res. 167 (2018) 223–233, https://doi.org/10.1016/j.envres.2018.07.010.
[10] A.-M. García, R.A. Torres-Palma, L.A. Galeano, M.Á. Vicente, A. Gil, Separation and characterization of NOM intermediates along AOP oxidation, in: A. Gil, L. A. Galeano, M.A. Vicente (Eds.), Applications of Advanced Oxidation Processes (AOPs) in Drinking Water Treatment, Springer, Cham, 2017, pp. 99–137, https://doi.org/10.1007/698_2017_128.
[11] J.H. Ramírez, L.A. Galeano, Natural organic matter removal by heterogeneous catalytic wet peroxide oxidation (CWPO), in: A. Gil, L.A. Galeano, M.A. Vicente (Eds.), Applications of Advanced Oxidation Processes (AOPs) in Drinking Water Treatment, Springer, Cham, 2017, pp. 69–98, https://doi.org/10.1007/698_2017_122.
[12] Y. Deng, R. Zhao, Advanced oxidation processes (AOPs) in wastewater treatment, Curr. Pollut. Rep. 1 (2015) 167–176, https://doi.org/10.1007/s40726-015-0015-z.
[13] M.A. Hassaan, A. El Nemr, Advanced oxidation processes for textile wastewater treatment, Int. J. Photochem. Photobiol. 2 (2017) 85–93, https://doi.org/10.11648/j.ijpp.20170101.15.
[14] E. Brillas, S. Garcia-Segura, Benchmarking recent advances and innovative technology approaches of Fenton, photo-Fenton, electro-Fenton, and related processes: a review on the relevance of phenol as model molecule, Sep. Purif. Technol. 237 (2019) 116337, https://doi.org/10.1016/j.seppur.2019.116337.
[15] S. Hussain, E. Aneggi, D. Goi, Catalytic activity of metals in heterogeneous Fenton-like oxidation of wastewater contaminants: a review, Environ. Chem. Lett. 19 (2021) 2405–2424, https://doi.org/10.1007/s10311-021-01185-z.
[16] E. Brillas, A review on the photoelectro-Fenton process as efficient electrochemical advanced oxidation for wastewater remediation, Treatment with UV Light, Sunlight, and Coupling with Conventional and Other Photo-Assisted Advanced Technologies, Chemosphere 250 (2020) 126198, https://doi.org/10.1016/j.chemosphere.2020.126198.
[17] J. Zhang, G. Zhang, Q. Ji, H. Lan, J. Qu, H. Liu, Carbon nanodot-modified FeOCl for photo-assisted Fenton reaction featuring synergistic *in-situ* H_2O_2 production and activation, Appl. Catal. B-Environ. 266 (2020) 118665, https://doi.org/10.1016/j.apcatb.2020.118665.
[18] M. Nguyen Van, O.L.T. Mai, C. Pham Do, H. Lam Thi, C. Pham Manh, H. Nguyen Manh, D. Pham Thi, B. Do Danh, Fe-doped g-C_3N_4: high-performance photocatalysts in rhodamine B decomposition, Polymer 12 (2020) 1963, https://doi.org/10.3390/polym12091963.
[19] C. Xu, P.R. Anusuyadevi, C. Aymonier, R. Luque, S. Marre, Nanostructured materials for photocatalysis, Chem. Soc. Rev. 48 (2019) 3868–3902, https://doi.org/10.1039/C9CS00102F.
[20] S. Sahar, A. Zeb, Y. Liu, N. Ullah, A. Xu, Enhanced Fenton, photo-Fenton and peroxidase-like activity and stability over Fe_3O_4/g-C_3N_4 nanocomposites, chinese, J. Catal. 38 (2017) 2110–2119, https://doi.org/10.1016/S1872-2067(17)62957-7.
[21] R. Shi, Y. Zhang, X. Wang, Q. Ma, A. Zhang, P. Yang, Electrospun $ZnFe_2O_4$ nanotubes and nanobelts: morphology evolution, formation mechanism and Fenton-like photocatalytic activities, Mater. Chem. Phys. 207 (2018) 114–122, https://doi.org/10.1016/j.matchemphys.2017.12.037.
[22] Q. Sun, Y. Hong, Q. Liu, L. Dong, Synergistic operation of photocatalytic degradation and Fenton process by magnetic Fe_3O_4 loaded TiO_2, Appl. Surf. Sci. 430 (2018) 399–406, https://doi.org/10.1016/j.apsusc.2017.08.085.
[23] J. Wen, J. Xie, X. Chen, X. Li, A review on g-C_3N_4-based photocatalysts, Appl. Surf. Sci. 391 (2017) 72–123, https://doi.org/10.1016/j.apsusc.2016.07.030.
[24] W.-J. Ong, L.-L. Tan, Y.H. Ng, S.-T. Yong, S.-P. Chai, Graphitic carbon nitride (g-C3N4)-based photocatalysts for artificial photosynthesis and environmental remediation: are we a step closer to achieving sustainability? Chem. Rev. 116 (2016) 7159–7329, https://doi.org/10.1021/acs.chemrev.6b00075.
[25] R. Zhang, X. Zhang, S. Liu, J. Tong, F. Kong, N. Sun, X. Han, Y. Zhang, Enhanced photocatalytic activity and optical response mechanism of porous graphitic carbon nitride (g-C_3N_4) nanosheets, Mater. Res. Bull. 140 (2021) 111263, https://doi.org/10.1016/j.materresbull.2021.111263.
[26] T. Ma, Q. Shen, B. Zhaoa, J. Xue, R. Guan, X. Liu, H. Jia, B. Xu, Facile synthesis of fe-doped g-C_3N_4 for enhanced visible-light photocatalytic activity, Inorg. Chem. Commun. 107 (2019) 107451, https://doi.org/10.1016/j.inoche.2019.107451.
[27] M.M. Desipio, S.E. Van Bramer, R. Thorpe, D. Saha, Photocatalytic and photo-Fenton activity of iron oxide-doped carbon nitride in 3D printed and LED driven photon concentrator, J. Hazard. Mater. 376 (2019) 178–187, https://doi.org/10.1016/j.jhazmat.2019.05.037.
[28] X. Jia, R. Dai, Y. Sun, H. Song, X. Wu, One-step hydrothermal synthesis of Fe_3O_4/g-C_3N_4 nanocomposites with improved photocatalytic activities, J. Mater. Sci.-Mater. El. 27 (2015) 3791–3798, https://doi.org/10.1007/s10854-015-4224-4.
[29] W. Luo, W. Huang, X. Feng, Y. Huang, X. Song, H. Lin, S. Wang, G. Mailhot, The utilization of fe-doped g-C_3N_4 in a heterogeneous photo-Fenton-like catalytic system: the effect of different parameters and a system mechanism investigation, RSC Adv. 10 (2020) 21876–21886, https://doi.org/10.1039/d0ra00993h.
[30] X. Qian, Y. Wu, M. Kan, M. Fang, D. Yue, J. Zeng, Y. Zhao, FeOOH quantum dots coupled g-C_3N_4 for visible light driving photo-Fenton degradation of organic pollutants, Appl. Catal. B-Environ. 237 (2018) 513–520, https://doi.org/10.1016/j.apcatb.2018.05.074.
[31] H.B. Truong, S. Bae, J. Cho, J. Hur, Advances in application of g–C_3N_4–based materials for treatment of polluted water and wastewater via activation of oxidants and photoelectrocatalysis: a comprehensive review, Chemosphere 286 (2022) 131737, https://doi.org/10.1016/j.chemosphere.2021.131737.
[32] S. Wang, Y. Liu, J. Wang, Iron and sulfur co-doped graphite carbon nitride (FeOy/S-g-C3N4) for activating peroxymonosulfate to enhance sulfamethoxazole degradation, Chem. Eng. J. 382 (2020) 122836, https://doi.org/10.1016/j.cej.2019.122836.
[33] X. Wang, W. Lu, Z. Zhao, H. Zhong, Z. Zhu, W. Chen, *In situ* stable growth of *β*-FeOOH on g-C_3N_4 for deep oxidation of emerging contaminants by photocatalytic activation of peroxymonosulfate under solar irradiation, Chem. Eng. J. 400 (2020) 125872, https://doi.org/10.1016/j.cej.2020.125872.
[34] C. Guan, J. Jiang, S. Pang, X. Chen, R.D. Webster, T.-T. Lim, Facile synthesis of pure g-C_3N_4 materials for peroxymonosulfate activation to degrade bisphenol a: effects of precursors and annealing ambience on catalytic oxidation, Chem. Eng. J. 387 (2019) 123726, https://doi.org/10.1016/j.cej.2019.123726.
[35] H. Li, C. Shan, B. Pan, Development of fe-doped g-C_3N_4/graphite mediated peroxymonosulfate activation for degradation of aromatic pollutants via nonradical pathway, Sci. Total Environ. 675 (2019) 62–72, https://doi.org/10.1016/j.scitotenv.2019.04.171.
[36] Y. Feng, C. Liao, L. Kong, D. Wu, Y. Liu, P.-H. Lee, K. Shih, Facile synthesis of highly reactive and stable fe-doped g-C_3N_4 composites for peroxymonosulfate activation: a novel nonradical oxidation process, J. Hazard. Mater. 354 (2018) 63–71, https://doi.org/10.1016/j.jhazmat.2018.04.056.
[37] J. Li, J. Fang, P. Ye, D. Wu, M. Wang, X. Li, A. Xu, Peroxymonosulfate activation by iron oxide modified g-C_3N_4 under visible light for pollutants degradation, J. Photoch. Photobio. A 342 (2017) 85–93, https://doi.org/10.1016/j.jphotochem.2017.04.004.
[38] Y. Li, N. Luo, Z. Tian, H. Li, M. Yang, W. Shang, S. Yifeng, M. Qu, A. Zhou, H_2O_2-free photo-Fenton degradation of organic pollutants on thermally exfoliated g-C_3N_4, Colloid. Surface A 586 (2019) 124190, https://doi.org/10.1016/j.colsurfa.2019.124190.
[39] H. Xu, Q. Ye, Q. Wang, P. Zhou, X. Huo, Y. Wang, X. Huang, G. Zhou, J. Zhang, Enhancement of organic contaminants degradation at low dosages of Fe (III) and H_2O_2 in g-C_3N_4 promoted Fe (III)/H_2O_2 system under visible light irradiation, Sep. Purif. Technol. 251 (2020) 117333, https://doi.org/10.1016/j.seppur.2020.117333.
[40] Y. Liu, Y. Zhao, J. Wang, Fenton/Fenton-like processes with in-situ production of hydrogen peroxide/hydroxyl radical for degradation of emerging contaminants: advances and prospects, J. Hazard. Mater. 404 (2020) 124191, https://doi.org/10.1016/j.jhazmat.2020.124191.
[41] S. Kumar, B. Kumar, A. Baruah, V. Shanker, Synthesis of magnetically separable and recyclable g-C_3N_4–Fe_3O_4 hybrid nanocomposites with enhanced photocatalytic performance under visible-light irradiation, J. Phys. Chem. C 117 (2013) 26135–26143, https://doi.org/10.1021/jp409651g.
[42] Y. Li, S. Zhu, Y. Liang, Z. Li, S. Wu, C. Chang, S. Luo, Z. Cui, Synthesis of α-Fe_2O_3/g-C_3N_4 photocatalyst for high-efficiency water splitting under full light, Mater. Des. 196 (2020) 109191, https://doi.org/10.1016/j.matdes.2020.109191.
[43] Z.I. Takai, M.K. Mustafa, S. Asman, K.A. Sekak, Preparation and characterization of magnetite (Fe_3O_4) nanoparticles by sol-gel method, Int. J. Nanoelectron. Mater. 12 (2019) 37–46.
[44] F.S. Yen, W.C. Chen, J.M. Yang, C.T. Hong, Crystallite size variations of nanosized Fe_2O_3 powders during γ-to α-phase transformation, Nano Lett. 2 (2002) 245–252, https://doi.org/10.1021/nl010089m.
[45] J. Rouquerol, F. Rouquerol, P. Llewellyn, G. Maurin, K.S. Sing, Adsorption by Powders and Porous Solids: Principles, Methodology and Applications, Academic press, 2014.
[46] D. Hernández-Uresti, A. Vázquez, D. Sanchez-Martinez, S. Obregón, Performance of the polymeric g-C_3N_4 photocatalyst through the degradation of pharmaceutical pollutants under UV–VIS irradiation, J. Photoch. Photobiol. A 324 (2016) 47–52, https://doi.org/10.1016/j.jphotochem.2016.01.031.
[47] N. Fairley, V. Fernandez, M. Richard-Plouet, C. Guillot-Deudon, J. Walton, E. Smith, D. Flahaut, M. Greiner, M. Biesinger, S. Tougaard, Systematic and collaborative approach to problem solving using X-ray photoelectron spectroscopy, Appl. Surf. Sci. Adv. 5 (2021) 100112, https://doi.org/10.1016/j.apsadv.2021.100112.
[48] N. Garkusheva, G. Matafonova, I. Tsenter, S. Beck, V. Batoev, K. Linden, Simultaneous atrazine degradation and *E. coli* inactivation by simulated solar photo-Fenton-like process using persulfate, J. Environ. Sci. Heal. A 52 (2017) 849–855, https://doi.org/10.1080/10934529.2017.1312188.
[49] L. Wang, Y. Hou, S. Xiao, F. Bi, L. Zhao, Y. Li, X. Zhang, G. Gai, X. Dong, One-step, high-yield synthesis of g-C_3N_4 nanosheets for enhanced visible light photocatalytic activity, RSC Adv. 9 (2019) 39304–39314, https://doi.org/10.1039/C9RA08922E.
[50] J. Liu, T. Zhang, Z. Wang, G. Dawson, W. Chen, Simple pyrolysis of urea into graphitic carbon nitride with recyclable adsorption and photocatalytic activity, J. Mater. Chem. 21 (2011) 14398–14401, https://doi.org/10.1039/C1JM12620B.

[51] M. Zhang, J. Xu, R. Zong, Y. Zhu, Enhancement of visible light photocatalytic activities via porous structure of g-C_3N_4, Appl. Catal. B: Environ. 147 (2014) 229–235, https://doi.org/10.1016/j.apcatb.2013.09.002.
[52] R.C. Dante, P. Martín-Ramos, A. Correa-Guimaraes, J. Martín-Gil, Synthesis of graphitic carbon nitride by reaction of melamine and uric acid, Mater. Chem. Phys. 130 (2011) 1094–1102, https://doi.org/10.1016/j.matchemphys.2011.08.041.
[53] J. Gao, Y. Wang, S. Zhou, W. Lin, Y. Kong, A facile one-step synthesis of fe-doped g-C3N4 nanosheets and their improved visible-light photocatalytic performance, ChemCatChem 9 (2017) 1708–1715, https://doi.org/10.1002/cctc.201700492.
[54] S. Xu, A. Habib, S. Gee, Y. Hong, M. McHenry, Spin orientation, structure, morphology, and magnetic properties of hematite nanoparticles, J. Appl. Phys. 117 (2015) 17A315, https://doi.org/10.1063/1.4914059.
[55] L. Qin, J. Meng, G. Yang, Y. Pan, X. Gao, Y. Yang, Y. Guo, Interlayer single-atomic Fe− N4 sites on carbon-rich graphitic carbon nitride for notably enhanced photo-Fenton-like catalytic oxidation processes towards recalcitrant organic micropollutants, Appl Catal B (2024) 123695, https://doi.org/10.1016/j.apcatb.2024.123695.
[56] D. Zhu, S. Liu, M. Chen, J. Zhang, X. Wang, Flower-like-flake Fe_3O_4/g-C_3N_4 nanocomposite: facile synthesis, characterization, and enhanced photocatalytic performance, Colloid. Surface A 537 (2018) 372–382, https://doi.org/10.1016/j.colsurfa.2017.10.053.
[57] J.M. Cho, M.H. Jeong, J.W. Bae, Fischer-tropsch synthesis on potassium-modified Fe_3O_4 nanoparticles, Res. Chem. Intermed. 42 (2015) 335–350, https://doi.org/10.1007/s11164-015-2360-3.
[58] L. Geng, B. Zheng, X. Wang, W. Zhang, S. Wu, M. Jia, W. Yan, G. Liu, Fe_3O_4 nanoparticles anchored on carbon serve the dual role of catalyst and magnetically recoverable entity in the aerobic oxidation of alcohols, ChemCatChem 8 (2016) 805–811, https://doi.org/10.1002/cctc.201501149.
[59] W. Jozwiak, E. Kaczmarek, T. Maniecki, W. Ignaczak, W. Maniukiewicz, Reduction behavior of iron oxides in hydrogen and carbon monoxide atmospheres, Appl. Catal. A-Gen. 326 (2007) 17–27, https://doi.org/10.1016/j.apcata.2007.03.021.
[60] L. Wan, D. Yan, X. Xu, J. Li, T. Lu, Y. Gao, Y. Yao, L. Pan, Self-assembled 3D flower-like Fe_3O_4/C architecture with superior lithium ion storage performance, J. Mater. Chem. A 6 (2018) 24940–24948, https://doi.org/10.1039/C8TA06482B.
[61] S. Ji, Y. Yang, Z. Zhou, X. Li, Y. Liu, Photocatalysis-Fenton of fe-doped g-C_3N_4 catalyst and its excellent degradation performance towards RhB, journal of water, Process. Eng. 40 (2021) 101804, https://doi.org/10.1016/j.jwpe.2020.101804.
[62] Y. Huang, X. Luo, Y. Du, Y. Fu, X. Guo, C. Zou, Y. Wu, The role of iron-doped g-C_3N_4 heterogeneous catalysts in Fenton-like process investigated by experiment and theoretical simulation, Chem. Eng. J. 446 (2022) 137252, https://doi.org/10.1016/j.cej.2022.137252.
[63] C. Ding, S. Kang, W. Li, W. Gao, Z. Zhang, L. Zheng, L. Cui, Mesoporous structure and amorphous fe-N sites regulation in fe-g-C_3N_4 for boosted visible-light-driven photo-Fenton reaction, J. Colloid Interface Sci. 608 (2022) 2515–2528, https://doi.org/10.1016/j.jcis.2021.10.168.
[64] J. Yang, H. Chen, J. Gao, T. Yan, F. Zhou, S. Cui, W. Bi, Synthesis of Fe_3O_4/g-C_3N_4 nanocomposites and their application in the photodegradation of 2,4,6-trichlorophenol under visible light, Mater. Lett. 164 (2016) 183–189, https://doi.org/10.1016/j.matlet.2015.10.130.
[65] A.M. García-Mora, C.S. Portilla-Delgado, R.A. Torres-Palma, A. Hidalgo-Troya, L.-A. Galeano, Catalytic wet peroxide oxidation to remove natural organic matter from real surface waters at urban and rural drinking water treatment plants, J. Water Proc. Eng. 42 (2021) 102136, https://doi.org/10.1016/j.jwpe.2021.102136.
[66] H.R. Devlin, I.J. Harris, Mechanism of the oxidation of aqueous phenol with dissolved oxygen, Ind. Eng. Chem. Fundam. 23 (1984) 387–392, https://doi.org/10.1021/i100016a002.
[67] L. Levy, A. Radian, Catechol-iron-clay surface complexation enriches radical formation and efficiency in heterogeneous Fenton reactions, Appl. Clay Sci. 232 (2023) 106802, https://doi.org/10.1016/j.clay.2022.106802.
[68] J. Bijlsma, W.J. de Bruijn, J.A. Hageman, P. Goos, K.P. Velikov, J.-P. Vincken, Revealing the main factors and two-way interactions contributing to food discolouration caused by iron-catechol complexation, Sci. Rep. 10 (2020) 8288, https://doi.org/10.1038/s41598-020-65171-1.
[69] C.-P. Huang, Y.-H. Huang, Comparison of catalytic decomposition of hydrogen peroxide and catalytic degradation of phenol by immobilized iron oxides, Appl. Catal. A 346 (2008) 140–148, https://doi.org/10.1016/j.apcata.2008.05.017.
[70] G. Zhang, Q. Wang, W. Zhang, T. Li, Y. Yuan, P. Wang, Effects of organic acids and initial solution pH on photocatalytic degradation of bisphenol a (BPA) in a photo-Fenton-like process using goethite (α-FeOOH), Photochem. Photobiol. Sci. 15 (2016) 1046–1053, https://doi.org/10.1039/c6 pp00051g.